Photorefractive Photonics and Beyond 2022

PR'22

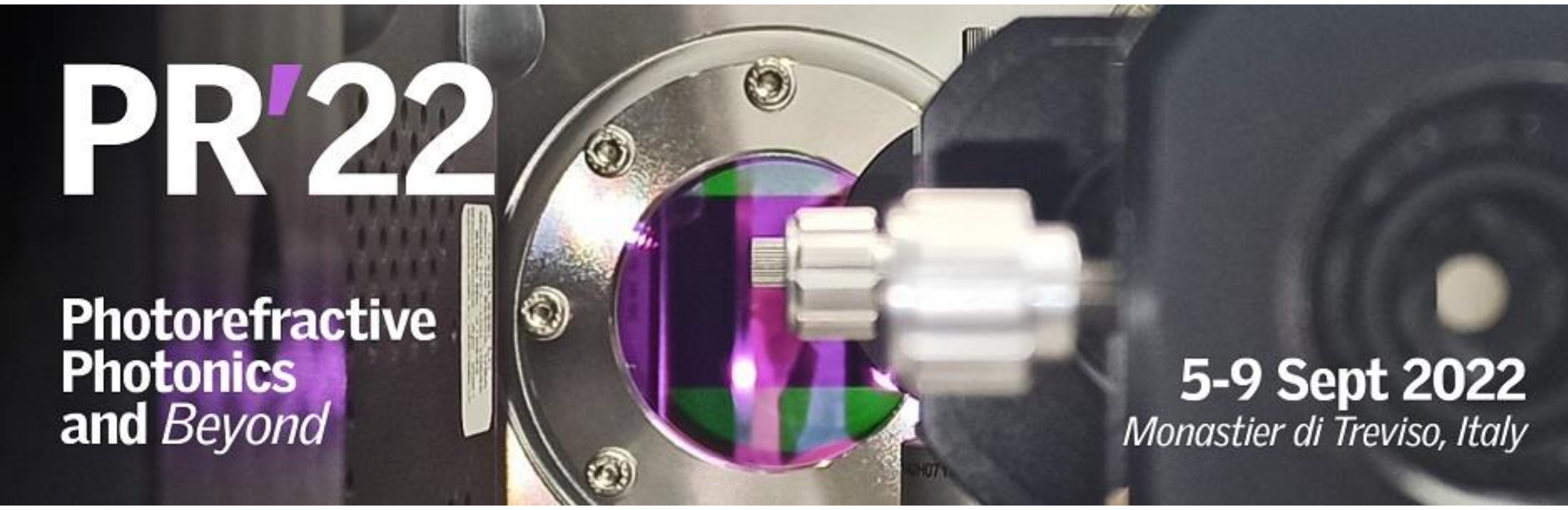

Book of papers

Contents

Addressable and erasable photonic neurons using solitonic X-junctions in lithium niobate thin films

A. Bile,[1] M.Chauvet,[2] F. Bassignot,[3] L. Gauthier-Manuel,[2] H. Tari,[1] E. Fazio,[1]

[1]Department of Fundamental and Applied Sciences for Engineering, Sapienza Università di Roma,
Via A. Scarpa 16, 00161 Roma, Italy,
, [2]FEMTO-ST institute, UMR CNRS 6174, University of Bourgogne Franche-Comté, 15B Avenue des Montboucons, 25030 Besançon, France,
[3]FEMTO-Engineering, 15B Avenue des Montboucons, 25030 Besançon, France.

Introduction

This paper reports the first implementation of an X-Junction structure made of lithium niobate thin films through the intersection of photorefractive soliton guides, which can act as photonic neurons by changing the signal addressing output according to an external control [1,2]. Moreover, we report the innovative discovery of the possibility of partially or totally erasing soliton structures in a targeted and selective way. The thin film acts as a planar waveguide for the input beams. The photorefractivity was controlled by the application of an external bias voltage generated through the pyroelectric effect [3,4] Therefore, the sample was placed on a feedbacked Peltier heater. The applied thermal gradient was of DT = 15 °C. During the heating procedure, the two beams were kept obscured to avoid any uncontrolled photorefractive effect in the crystal. In figure 1 (a) the light distribution at the output face is reported: in particular, figure 1 (a_1) shows the free-diffracting behaviors of the beams. However, when the propagation occurs at the same time as the excitation of the nonlinearity, the beams begin the self-focusing process. The X-junction can change the distribution of an injected signal (characterized by powers of the order of nW) towards the two output channels as a function of the writing power. If the input powers are equal, $W_1 = W_2$, the written structure results balanced. In this case, the signal inserted by one of the input channels will split equally to 50% in the two output channels, as represented by figure 1 (a_2). Instead, if the writing power of one channel is higher than the other, the resulting X-junction is unbalanced towards one specific output. By setting the highest power two times the other, the signal switches asymmetrically 70-30 towards the strongest channel, shown in figure 1(a_3); by setting the highest power triple than the other, the signal switches again towards the strongest channel, but asymmetrically 80-20 (figure 1(a_4)). We have observed that whatever structure is written, it is possible to carry out an erasing procedure to bring the crystal back to initial conditions and thus perform new experiments. To erase the written solitonic waveguides, the lasers are obscured and the Peltier is turned off so that the crystal temperature returns to the ambient one (DT = 0). This operation allows to annul the thermal gradient At this point an input laser is activated, in the same position it had at the time of writing, with an input power about 80 times higher. Typical writing powers that have been used are of the order of 10 mW which allow the formation of soliton waveguides in a time of the order of 5 min. This produces a fast movement of charge which is homogeneously redistributed throughout the crystal, canceling the local refractive index contrast at the base of the solitonic structures. Figure 1 (b) shows 4 frames relating to the erasing process of an unbalanced X junction with left channel characterized by a higher index contrast. Frames were chosen to well show the induced variation both in the short-term time range (within 1 min after having started the process and in the long term, (beyond 1 min). Observing the evolution of the structure, the channel characterized by a stronger refracrtive index modification requires a longer erasing time.

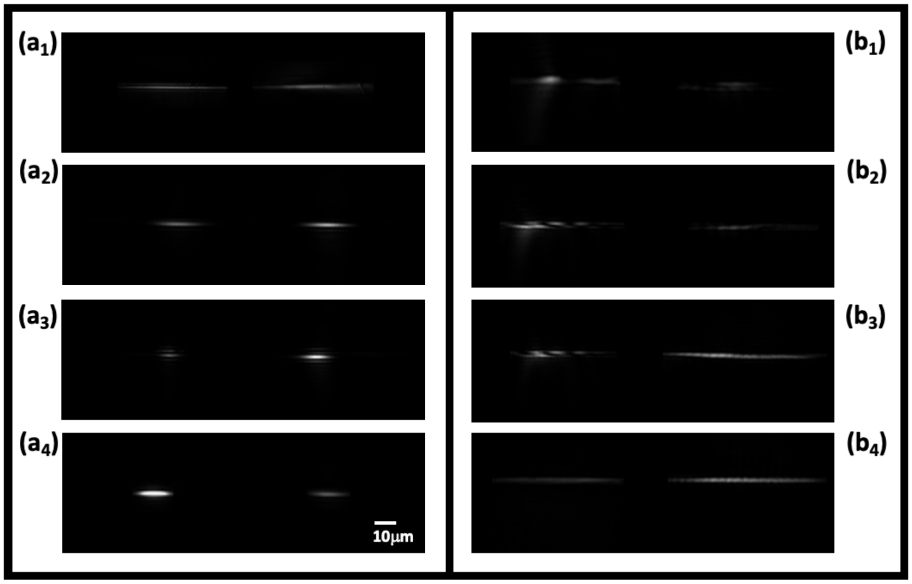

Figure 1: Light distribution at the output face is reported. (a) the signal-switching behaviors after writing phase is shown: (a_1) initial diffracting beams in linear regime; (a_2) writing with same intensities beams produces a balanced X-Junction which split signal 50-50 towards the outputs; (a_3) if the right channel is written with double intensity with respect to the other, the signal split is 70% in his favour; (a_4) if the left channel is written with tirple intensity with respect to the other, the signal split is 70% in his favour. (b) the erasing process of an unbalanced X-Junction on the left is shown with subsequent frames (b_1-b_4).

Conclusions

We have experimentally shown the formation all-optical addressable X-junctions in slab waveguides of LiNbO3 by using pyroelectric effect for self-focusing mechanism, which are able to switch the energy addressing towards outputs and to be partially or totally erased. The behavior illustrated is typical of biological neurons. Thus, X-Junctions in lithium niobate thin film can act as photonic neurons.

References

[1] M. Alonzo, D. Moscatelli, L.Bastiani, A.Belardini, C. Soci and E. Fazio.. Sci. Rep. **8**, 5716 (2018).
[2] A. Bile, F. Moratti, H. Tari, E. Fazio, Neural Comput & Applic **33,** 17071 (2021).
[3] M.G. Vazimali, S. Fathpour, Adv. Phot. **4**, 034001 (2022).
[4] M. Chauvet, F. Bassignot, F. Henrot, F. Devaux, L. Gauthier-Manuel, H. Maillotte, G. Ulliac, B. Sylvain, Opt. Lett. **40**, 1258 (2015).

All-optical switching on plasmonic-lithium niobate metasurfaces

Artemios Karvounis, Helena Weigand, Martin Varga, Viola V. Vogler-Neuling, Rachel Grange

ETH Zurich, Department of Physics, Institute for Quantum Electronics, Optical Nanomaterial Group
Zurich, Switzerland

Introduction

Photonic integrated circuits (PICs) and flat optics rely on passive optical elements made from high index dielectrics, (eg silicon and silicon nitride) or plasmonic metals.[1] Phase change materials,[2]and nano-mechanical systems[3] have been the major material platforms to realise active nonlinearities and reconfigurable optical elements. However, such systems are difficult to incorporate with PICs. In this work, we report a method for flat all-optical switches based on lithium niobate ($LiNbO_3$) substrates, as we exploit photogalvanic and photorefractive effects to develop all-optical switchable metasurfaces on $LiNbO_3$ substrates.

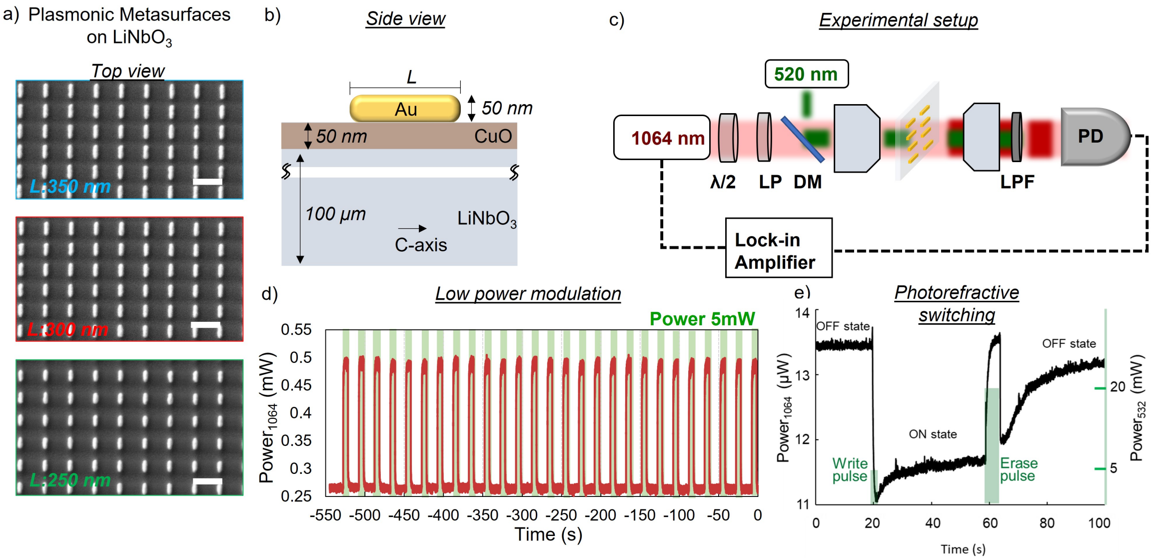

Figure 1: a) Top view SEM images of the plasmonic nano-bar arrays of various length (L) as annotated, scale bar: 400 nm. b) Schematic side view of a single unit cell with annotated dimensions of each film. c) Experimental setup of the characterisation setup. $\lambda/2$: half-waveplate, LP: linear polariser, DM: dichroic mirror, HPF: High pass filter, PD: photodiode. d) Stable all-optical switching performed over many repetition cycles, shaded green areas corresponds to the timeframe that the pump laser is ON. e) Two-level memory system of optical bits encoded on the transmission level of the metasurface. The pump pulses of different duration and power perform the write and erase function, while the probe beam is used for the reading.

Methods/Results

The metasurfaces consist of periodic arrays (fixed period at 400 nm) of gold nano-bars of variable length. The plasmonic metasurfaces are produced by top-down methods. After depositing a thin layer of Au, namely 50 nm on a CuO/$LiNbO_3$ substrate, the Au films are patterned via FIB milling. The SEM images of the fabricated samples, as well as the schematic of a single unit cell, are presented in figure 1a and b, respectively. A pump-probe setup was built based on a inverted microscope to perform the all-optical switching. The probe laser (1064 nm) is electrically modulated at 1 KHz via a lock-in amplifier, while the pump beam (520 nm) is a diode laser of variable pulse width controlled by a function generator. A pair of objectives is used to focus the laser beams on the samples and to collect the probe beam in an InGaAs photodiode.

The transmission level of the metasurface at the probe wavelength is modified by the green laser, as presented in Figure 1 d and e. The plasmonic metasurfaces introduce optical absorption at the wavelength of the green laser, while at the probe wavelength the switching ratio is controlled by the length of the Au nano-bars. The absorbed light result in the carrier generation and thermal expansion, thereby the opto-thermal heating in combination with the photogalvanic effect, induce the motion of charges, that alter the optical properties of the metasurfaces. In low power regime, we have managed to record transmission contrast ratio up to 2.2:1, see Figure 1d.

For the samples that we have annealed at 800 ^oC before the deposition of Au, we record a different response. The transmission changes are not reversible as before, but irreversible. We can explain this behaviour as the thermal diffusion of Cu in the $LiNbO_3$ lead to the generation of deep carriers that give rise to this type of photorefractive switching. The transmission contrast is polarisation dependent and is associated with the orientation of the polarisation of the probe beam with the c-axis of the substrate, while the photorefractive switching is recorded for light polarised parallel to the c-axis.

Conclusions

We have presented a novel method to perform all-optical switching in flat photonic architectures based on the combination of photonic metasurfaces with $LiNbO_3$ substrates. The reversible and irreversible transmission contrast between different types of samples paves the way for a new family of adaptive optical devices based on the $LiNbO_3$ platform. The transmission contrast ratio of 2.2:1 demonstrated here is already adequate for short-reach (intra-/interchip) optical interconnect applications in data processing architectures.[1] The plasmonic metasurfaces may form essential functions such as optical modulators and/or optical waveplates towards the development of optical components with active tuning capabilities. Furthermore, the rewritable optical properties could be used in planar switchable optical devices.

References

[1] G. Reed, G. Mashanovich, F. Gardes et al. Nature Photon **4**, 518–526 (2010)

[2] A. Karvounis, B. Gholipour, K.F.MacDonald, N.I.Zheludev Appl. Phys. Lett. **109**, 051103 (2016)

[3] A. Karvounis, N. Aspiotis, I. Zeimpekis, et. al. Adv. Sci. **6**, 1900974 (2019)

Cancer Holography for Personalized Medicine

David D. Nolte

Department of Physics, Purdue University,
West Lafayette, IN 47907, USA

Introduction

Digital holography opens new opportunities for personalized medicine by measuring the three-dimensional physiology and motion of cancer cells and by identifying effective chemotherapies for cancer patients. Off-axis holographyuses an off-axis reference wave to produce an interference fringe pattern on a digital light sensing array like a CCD or CMOS camera chip is called digital holography, illustrated in Fig. 1.

The advantages of holography are well-suited for three dimensional cell tracking to measure the movement of cells, such as metastatic cancer cell migration, through translucent three-dimensional biological matrix samples [1]. Although single cells or small numbers in 3D biological matrices are transparent and can be imaged in transmission, dense layers of cells thicker than even a tenth of a millimeter no longer transmit much light and other methods are needed.

Thick cancer tissues, such as biopsy specimens, are translucent but attenuate light, preventing their interrogation with transmission holography. Backscattering of light from thick tissues can be relatively bright, allowing the use of light ranging techniques to measure the optical path distance that the light has traveled. Although time-of-flight measurements of reflected light pulses are not practical, optical path-length differences are measured easily using a coherence-gated approach. Coherence-gated digital holography matches the optical path lengths of light scattered from tissue relative to a second delayed reference wave. Off-axis coherence-gated digital holography measures *spatial* interference on a pixel array by imaging holographic fringes at a fixed path length [2]. This is in contrast to optical coherence tomography (OCT) that uses rapid path-length scanning or swept sources to produce *temporal* heterodyne signals.

Intracellular Doppler Spectroscopy

The speeds of cellular and intracellular components inside living tissue span from tens of nanometers per second (slow membrane shape changes and cell motility) to tens of microns per second (fast organelle and vesicle traffic inside a cell). In the near-IR using a light-backscatter configuration, these speeds produce Doppler frequency shifts from 10 mHz to 10 Hz, respectively. At the ultra-low-frequency (ULF) range of 10 mHz, this represents an impressive frequency shift of one part in 10^{16} on the central frequency of the probe light. This extreme sensitivity is beyond the capabilities of direct frequency measurement but is made possible through interferometric phase-sensitive detection. Therefore, the most sensitive approach to characterize intracellular dynamics is through high-dynamic-range speckle fluctuations [3].

In this presentation, I will describe a prospective multi-center observational study that enrolled treatment-naïve adult breast cancer patients who subsequently received standard-of-care neoadjuvant chemotherapy at four breast cancer centers in the United States. Participants were recruited by each investigator in a consecutive series beginning in February 2017. There were 72 patients who completed neoadjuvant treatment with subsequent surgical intervention through November 2019. Two standard-of-care combination therapy regimens were evaluated in the study: 1) anthracycline-based therapy, typically followed by a taxane (AC-T) and 2) non-anthracycline therapy, specifically Taxotere® (TC).

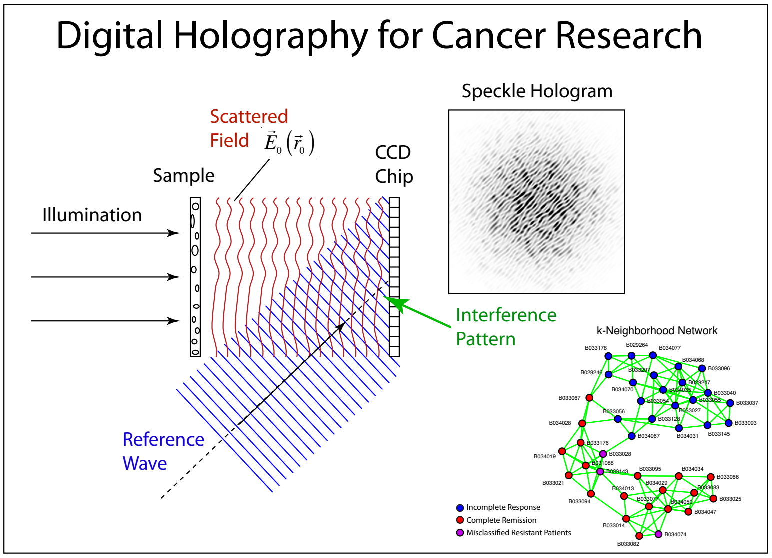

Fig. 1 Principles of digital holography (DH). In digital holography a pixel array (CCD) records the interference fringes of light scattered from a biological sample interfering with a reference wave (off-axis angle exaggerated) to form a speckle hologram. The network shows the classification of breast cancer patients into patient cohorts who are sensitive or resistant to their cancer therapy

For each patient, biodynamic signatures were developed for all combination therapies, component monotherapies, and negative controls (culture medium + 0.1% dimethyl sulfoxide). Patients were followed through surgical intervention (mastectomy or lumpectomy) and outcomes were classified by central pathology review using scoring standards. A Siamese Deep Learning network was trained on the biodynamic data using patient outcomes to provide likelihoods of cancer remission for each patient and each therapy.

Conclusions

Holographic recording of dynamic speckle from tumor biopsies undergoing medical treatment opens a new area of applications for holographic techniques, including photorefractive approaches, in biomedical optics.

References

1. X. Yu, J. S. Hong, C. G. Liu, and M. K. Kim, *Optical Engineering,* vol. 53, no. 11, Art no. 112306 (2014)
2. K. Jeong, J. J. Turek, and D. D. Nolte, *Optics Express,* vol. **15**, pp. 14057-14064, (2007)
3. P. Yu, L. Peng, M. Mustata, J. J. Turek, M. R. Melloch, and D. D. Nolte, *Optics Letters,* vol. 29, pp. 68-70, (2004)

Composition dependent optical properties of $LiNb_{1\text{-}x}Ta_xO_3$ solid solutions

Felix Bernhardt[1], Florian Pfeiffer[1] and Simone Sanna[1]

[1]Institut für Theoretische Physik and Center for Materials Research
Justus-Liebig-Universität Gießen, 35392 Gießen, Germany

Introduction

Lithium niobate (LN) and lithium tantalate (LT) are ferroelectric crystals with a wide range of applications, extending from piezoelectric sensors [1] to integrated photonics [2]. Their structural similarities enable the combination of these materials to $LiNb_{1\text{-}x}Ta_xO_3$ (LNT) alloys. As the optical absorption edge depends on the stoichiometry, this property can be used to determine the crystal composition non destructively.

Here, we use *special quasi-random structures* (SQS) to simulate LNT crystals with different compositions. These structures mimic an ideal random alloy, even when periodic boundary conditions are employed. Furthermore, we use the Li-vacancy model as well as the Nb-antisite model to simulate congruent LN crystals, as these crystals are commonly used in experiments.

We calculate the first order dielectric tensor of both materials by using *density functional theory* (DFT) and the *indepent particle approximation* (IPA).

Methodology

For all of our calculations we are using DFT as implemented in VASP [3, 4]. The pseudopotentials are given in the PBEsol formulation [5, 6].

Utilizing the orthorhombic $2 \times 1 \times 1$ supercell of LN as a starting point for our simulations, we gradually exchange the Nb atoms with Ta atoms. This procedure is carried out such, that the correlation between Ta occupation sites, as defined in Ref. [7], is minimzed. Thus, we obtain 22 SQS of the LNT crystal. Their Ta concentration ranges from 4.2 % to 95.8 %.

For modelling congruent LN, we use cells as large as up to $4 \times 4 \times 4$ rhombohedral supercells, removing up to four Li^+ from these structures. This creates Li^+-vacancy concentrations of as low as 0.78 %. Also, we employ the Nb-antisite model as described in Ref. [8]. Additionally, we use a GGA+U scheme for the Nb d electrons to correct for the underestimation of the electronic band gap in DFT. For all of these structures we optimize the ionic positions and the volume, employing the Murnaghan equation of states for the latter. To calculate the dielectric function, we use the IPA as implemented in VASP. The absorption edge is then extracted by a linear fit of the first peak in the imaginary part of the dielectric function.

Results

Our calculations show a clear dependence on the absorption edge with respect to the Nb/Ta ratio of the LNT crystals. The absorption edge increases with increasing Ta concentration. This behaviour holds for all diagonal components of the dielectric tensor and might be explained by the electronic DOS: LT features a higher absorption edge than LN [9], and mainly the states corresponding to Nb and Ta directly above the Fermi-energy change, with the Ta-states featuring slightly higher energies. As the bands near the Fermi-energy are mostly flat throughout the Brillouin-zone and we only consider direct transitions in the IPA, this corresponds to a higher absorption edge in LT than in LN.
For congruent LN, we also observe a non-linear behaviour of the absorption edge with respect to the Li^+-vacancy concentration for all diagonal components of the dielectric function, as has been reported in [8, 10]. Here, the Nb states in the lower valence bands are shifted to smaller energies with increasing Li^+-vacancy concentration.

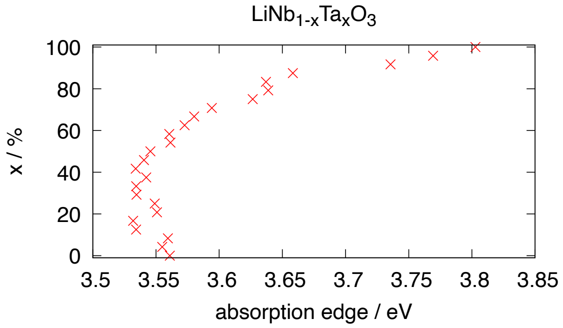

Figure 1: Absorption edge of LNT with respect to Nb/Ta ratio. Only The xx-component of the dielectric tensor has been considered.

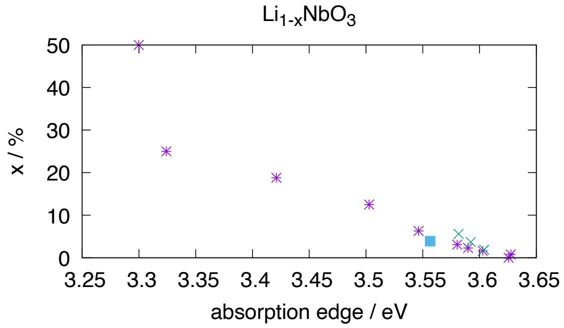

Figure 2: Absorption edge of LN with respect to Li^+-vacancy concentration. Only The xx-component of the dielectric tensor has been considered. The green crosses denote calculation with higher numerical accuracy, whereas the blue cube represents the Nb-antisite model.

Conclusion

The absorption edge of LNT crystals with different Nb/Ta ratios was calculated. We determine a clear trend, that the absorption edge increases with increasing Ta concentration. We also note, that the absorption edge of LN decreases with increasing Li^+-vacancy concentration. These results are in qualitative agreement with experimental measurements.

References

[1] M. Xu *et al*, ACS Appl. Mater. Interfaces **9**, 40, (2017)

[2] W. Sohler *et al*, Optics & Photonics News **19**, 1, (2008)

[3] The VASP site, `https://www.vasp.at/`

[4] G. Kresse *et al.*, Phys. Rev. B **59**, 3, (1999)

[5] J. Perdew *et al.*, Phys. Rev. Lett. **77**, 18 (1996)

[6] J. Perdew *et al.*, Phys. Rev. Lett. **100**, 13, (2008)

[7] A. van de Walle *et al.*, Calphad **42**, 13-18 (2013)

[8] Y. Li *et al.*, Phys. Rev. B **91**, 17 (2015)

[9] S. Çabuk *et al.*, J. Opt. A **1** 424, (1999)

[10] K. Polgar *et al.*, Journal of Crystal Growth **177** 211-217, (1997)

Conical diffraction cascades and interplay with linear and nonlinear material properties

Muhammad Waqar Iqbal[1,2], Yulija Shiposh[3], Anton Kohutych[3], Nicolas Marsal[1,2],
Alexander Grabar[3], and Germano Montemezzani[1,2]

[1] Université de Lorraine, CentraleSupélec, LMOPS, 57000 Metz, France
[2] Chair in Photonics, CentraleSupélec, LMOPS, 57000 Metz, France
[3] Inst. for Solid State Physics and Chemistry, Uzhhorod National Univ., 88000 Uzhhorod, Ukraine

Introduction

Internal conical diffraction is a well-known singular phenomenon observable whenever a tightly focused wave is incident with its wavevector along one of the two optical axes of an optically biaxial crystal [1]. The effect gives rise to a vector type wave with the Poynting vectors associated to each linear polarization component lying on a slanted cone surface with circular base. The number of these cones can be multiplied by a factor $2^{N\text{-}1}$ if a cascade of N biaxial crystals with perfectly aligned optical axes is considered. When observed on a plane perpendicular to the optical axis, these structures have a circular form. However, as it will be discussed in this contribution, a dramatic change in the shape of the conical diffraction vector beams can be achieved if a proper manipulation in wavevector space is performed between the different crystals in a cascade. Highly peculiar non-circularly shaped vector beams can be obtained, some of which associated to a reversed curvature as compared to the one proper to circles [2].

Results

Figure 1 illustrates the concept, the schematic set-up and two examples of obtained conical diffraction beams for a cascade of two crystals. In the case of Fig. 1(c) only the magnitude, but not the direction, of the transverse component of the wavevector is being manipulated (by means of a spherical lens between the two biaxial crystal). This correspond to the so-called “variable cascade” introduced earlier by Peet [3] and leading still to circularly shaped structures. In contrast, the use of two crossed cylindrical lenses permits an anisotropic imaging in the transverse x and y directions between the planes FIP1 and FIP2 in Fig. 1(b). This leads to the mentioned non-circular vector beams, as seen in the example of Fig. 1(d). For such patterns the type of curvature can be predicted on the base of the material optical properties, the sample lengths, and the x and y magnification factors M_x and M_y provided by the cylindrical lenses. The same is true for the positions of the intersection points of the structures with the x and y transverse axes.

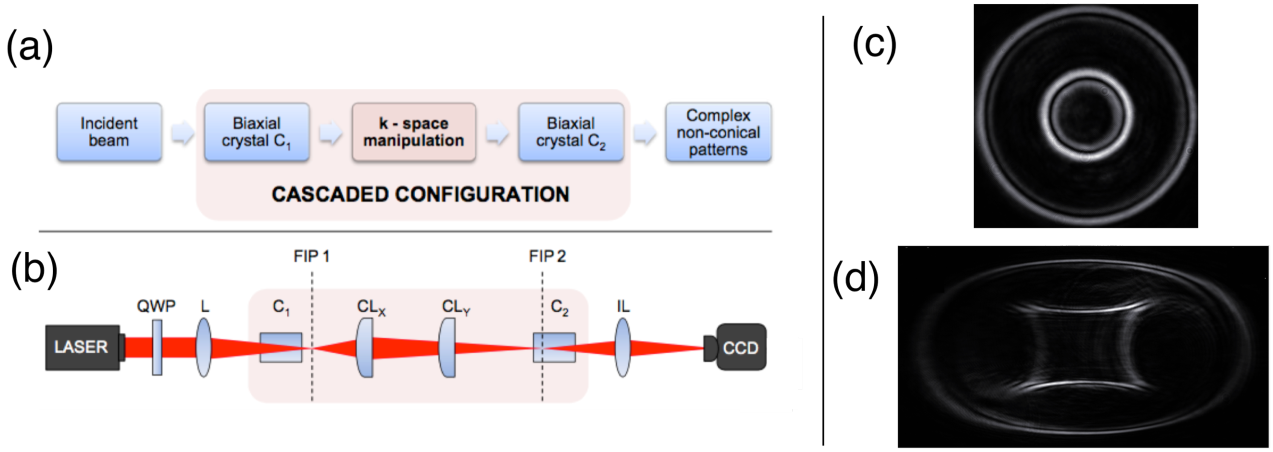

Figure 1: Concept (a) and experimental set-up (b) of a cascaded conical diffraction with manipulation in wave-vector space between two optically biaxial crystals (C_1, C_2) in cascade. QWP is a quarter-wave plate, L and IL are a focusing and imaging spherical lens, respectively, and CL_x and CL_y are crossed cylindrical lenses. Panel (c) shows an example of the obtained pattern (at plane FIP 2) when the two intermediate cylindrical lenses are replaced by a single spherical lens (variable cascade), what conserves the pattern circular symmetry. In (d), in contrast, a wave-vector manipulation by the crossed cylindrical lenses leads to peculiar non-circular patterns with the internal structure having a reversed curvature (see [2] for more details and theoretical approach).

In the standard circular case with only one crystal, the circle radius is uniquely determined by the values of the three principal refractive indices of the biaxial crystal and by the length of the sample. However, conical diffraction in both single step and cascaded configurations can be influenced also by other linear and eventually nonlinear optical properties of the involved crystals (optical activity, photoinduced effects, …). Such an interplay is discussed in the case of photorefractive $Sn_2P_2S_6$ crystals [4], as compared to standard materials commonly used for conical diffraction, such as centrosymmetric $KGd(WO_4)_2$. The potential role of photorefractivity in view of a conical diffraction holography will also be discussed.

References

[1] A. Turpin, Y. V. Loiko, T. K. Kalkandjiev and J. Mompart, Laser Photonics Rev. **10**, 750–771 (2016).
[2] M. W. Iqbal, N. Marsal and G. Montemezzani, Sci. Rep. **12**, 7317 (2022).
[3] V. Peet, Opt. Lett. **40**, 2405–2408 (2015).
[4] A. A. Grabar, Yu. M. Vysochanskii, A. Shumelyuk, M. Jazbinsek, G. Montemezzani and P. Günter, "Photorefractive effects in $Sn_2P_2S_6$", in "Photorefractive materials and their applications. Vol. II: Materials", P. Günter and J. P. Huignard Eds., (Springer, New York, 2007), pp. 327-362.

Controllable waveguiding structures induced by diffracting Bessel beams in a nonlinear medium

Yue Chai,[1] Nicolas Marsal,[1] Delphine Wolfersberger[1]

[1]Chair in Photonics, CentraleSupélec, LMOPS, 2 Rue Edouard Belin, 57070 Metz, France

Introduction

Due to their unique profiles and fascinating propagating phenomena, unconventional beams like Airy beams are good candidates for photo-inducing waveguiding structures in for example a photorefractive medium. Bessel beams (BBs) share similar features with Airy beams, such as diffraction-free, multi-lobes profiles, and self-trapping properties under nonlinear conditions. Thus, several studies on waveguides induction using non-diffracting BBs under weak nonlinearity have been developed [1]. Instead, our recent work unveiled that diffracting BBs propagating under high nonlinear conditions provide more advantages and opportunities for fully controllable waveguiding structures.

Results and discussion

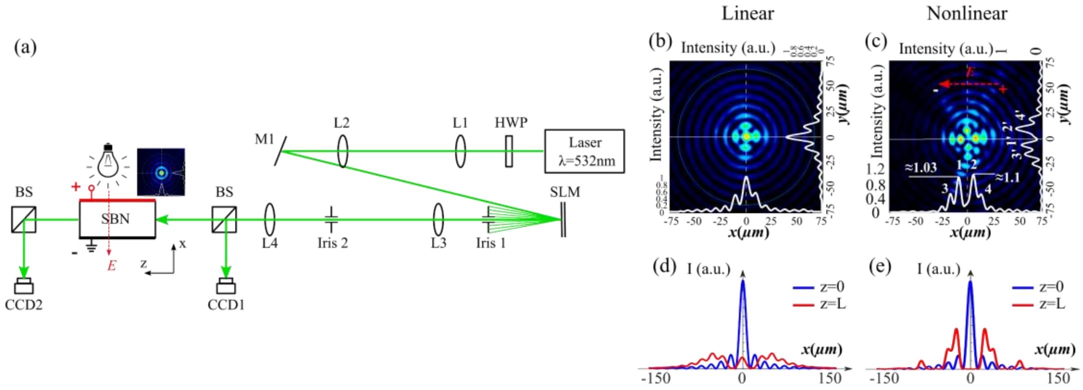

Figure 1: (a) Experimental setup: HWP, half-wave plate; L, lens; M, mirror; SLM, spatial light modulator; BS, beam splitter. (b)(c): Output profiles of a 6 µm zero-order BB propagating under (b) linear conditions and (c) nonlinear conditions. (d)(e) Corresponding numerical results of the diffracting BB.

Our experiment consists of propagating a single zero-order BB in a PR strontium barium niobate crystal (SBN: Ce) with the dimension of $0.5 \times 0.5 \times 1$ cm, as depicted in Fig. 1(a). The BB is generated by a SLM and reduced by lenses (L3, L4) then launched into the SBN crystal. An external electric field is applied along the crystallographic c axis of the crystal for activating the nonlinearity. The input and output profiles are monitored by the CCD1 and CCD2 cameras. Figures 1(b) and 1(c) are the output profiles of a 6µm BB propagating in the biased SBN crystal [2]. The profile in Fig. 1(b) is no longer the same as the input BB profile, suggesting that the BB diffracts and distorts during its linear propagation in the 1cm crystal. When we apply the electric field to the crystal, as shown in Fig. 1(c), the central peak disappears, and the optical energy shifts to the adjacent lobes (1, 2, 3, 4). On the other hand, we developed the 1D numerical model to verify our experimental results and investigated more interesting waveguiding structures. We restricted the BB in the 1D situation where the transverse direction corresponds to the c axis of the PR crystal. The propagation of the BB in the crystal is described by $i\partial_Z F+\partial^2_X F = \Gamma E_0 F$, where Γ is the nonlinear strength [3]. Figures 1(d) and 1(e) show the 1D profiles of a diffracting BB propagating under linear and nonlinear conditions. We notice that our experimental results are in good agreement with our 1D numerical results.

It is worth noting that our all-optical platform owns several parameters such as BB size, BB order, BB truncation, the external electric field, input Bessel beam intensity, and background illumination. By adjusting these parameters, we can tailor the photo-induced waveguiding structures. For example, in the experiments, as shown in Fig. 2(a), we obtain the waveguiding structures with 5, 9, and 8 potential addressable outputs as increasing the nonlinearity. Moreover, when we fix the electric field at 3.8 kV/cm and increase only the input intensity, as shown in Fig. 2(b)-2(d), the intensity difference between outputs (1,2) tends towards 0. In this case, the guiding efficiency of each photo-induced channel is tailored by the input intensity.

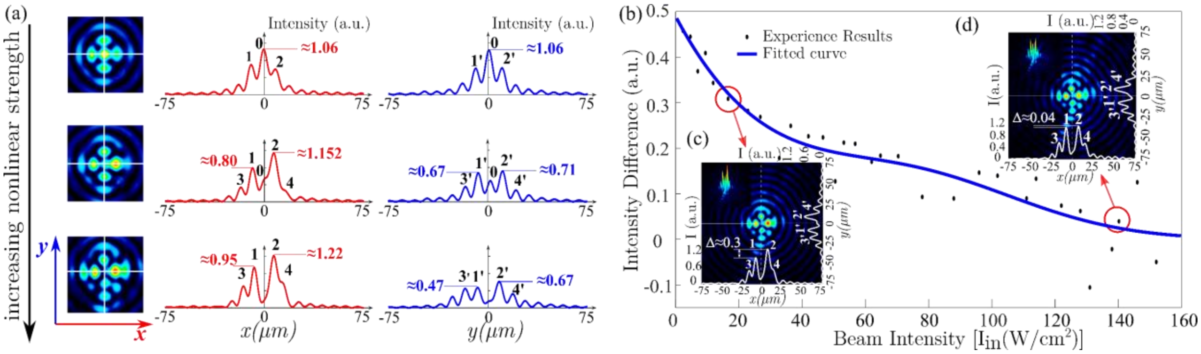

Figure 2: (a) 2D intensity distributions of the outputs, their corresponding profiles along x and y directions when a 6μm BB propagates for increasing nonlinearity. (b) Difference of the intensities between outputs (1,2) versus the input intensity. (c)(d) Two examples for low and high input intensities.

Conclusion

We numerically and experimentally demonstrated that a single diffracting BB could induce the waveguiding structures with multiple channels in a biased PR crystal. By varying the parameters of the BB and the nonlinearity of the crystal, our platform can tailor the output numbers, the guiding efficiency, and the stability of the waveguiding structures. These results provide more complex waveguiding structures and further possibilities for all-optical interconnects.

References

[1] F. Xin, M. Flammini, F. Di Mei, L. Falsi, D. Pierangeli, A. J. Agranat and E. DelRe, Physical Review Applied, 11(2), 024011 (2019)
[2] Y. Chai, N. Marsal, and D. Wolfersberger, Physical Review Applied 17.6 064063 (2022)
[3] Y. Chai, N. Bouldja, N. Marsal, and D. Wolfersberger, Optics Express 29, 40231 (2021)

Defect detection in composite material by means of photorefractive vibrometry

Tommaso Seresini[1], Wei Qi[1], Peilong Yuan[1], Liwang Liu[1] Helge Pfeiffer[2], Martine Wevers[2]
Christ Glorieux[1]

[1]Soft Matter and Biophysics Laboratory, Celestijnenlaan 200D, Leuven, Belgium,
[2]Department of Materials Engineering, Kasteelpark Arenberg 44, 3001, Leuven, Belgium

The use of composite materials for structural elements in high value structures and components (e.g., wind turbines blades, composite parts in aircrafts …) requires fast and reliable tools for assessing their structural integrity.

The inspection method proposed in this work is based on the detection of defect-induced elastic cross-modulation phenomena using a vibrometric scheme that makes use of photorefractive interferometry. This non-contact method is full-field and aims at inspecting large areas at once and enable detection of defects in an early stage.

The novelty of the system lies in both the acoustic excitation and in the detection method. Two guided waves are sent along the sample: one of low amplitude and high frequency (probe) and one of high amplitude and low frequency (pump). The mechanical response of a damaged composite sample is, in general, not linear. Detection of acoustic frequency mixing caused by mechanical nonlinearity can thus evidence the presence of a crack or delamination defect.

We have exploited non-degenerate two-wave mixing in a photorefractive crystal to perform a full-optical lock-in detection and image the vibration pattern at the frequency of interest, the defect signature, without crosstalk from other vibrations, e.g., from the strong pump vibration, which was used to modulate the defect response to probe vibrations.

Using standard homodyne interferometry, frequency mixing between the modulation frequency and the probe frequency, resulting from the defect response would be indistinguishable from frequency mixing due to the nonlinear relation between the interferometer light intensity and the measured displacements. Heterodyne techniques, on the other hand, do not allow for full field detection. This work highlights that photorefractive interferometry allows for frequency selective detection of vibrations and enables to identify the modulated probing signal amid an intense vibration background.

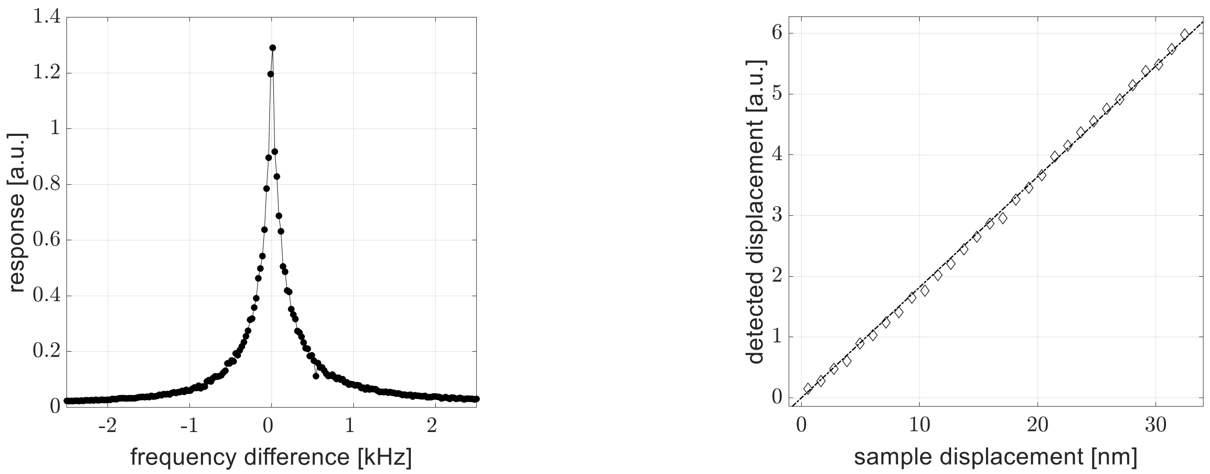

Figure 1, left. PRI response as a function of the frequency difference between the target frequency and the frequencies at which the sample vibrates. The PRI response is that of a bandpass filter. Right, detected displacement as a function of sample displacement. The PRI has a linear response and a minimum detectable displacement of 0.5 nm

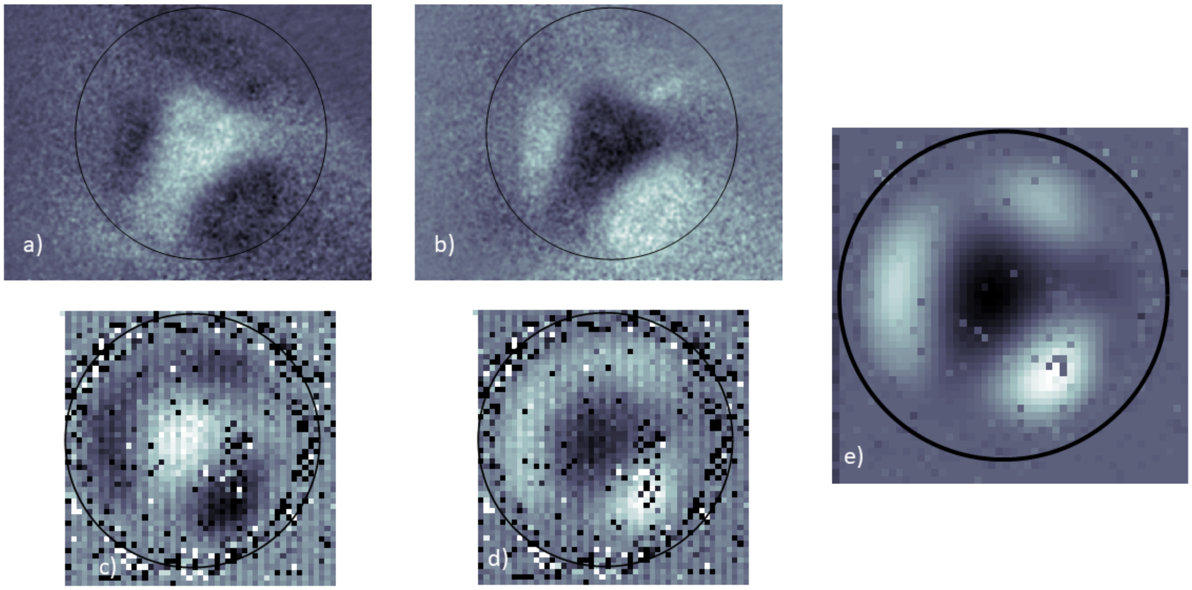

Figure 2 Vibration modes of a brass plate, coupled to a piezo actuator, as imaged by the PRI (a,b) compared to as measured by a commercial laser Doppler Vibrometer (c,d,e). The brass plate is a disc of 4 cm diameter, clamped at the edge (black solid circle). Panels a) and b) snapshots of the vibration pattern at a standing mode of the sample (2400 Hz) at phase= 0° (a) and 180° (b). Panels c) and d) are obtained by scanning the sample with a laser Doppler vibrometer at phase= 0° (c) and 180° (d). Panel e) is the Fourier transform of the laser Doppler scan calculated at 2400Hz. The sample vibration amplitude was 90 nm.

High-Performance Co-Doped Photorefractive $Sn_2P_2S_6$ Crystals

Alexander Grabar, Mykhailo Tsyhyka, Anton Kohutych,
Konstantin Glukhov, Stepan Hasynets

Institute for Solid State Physics and Chemistry, Uzhhorod National University,
Pidhirna Street 46, Uzhhorod, 88000, Ukraine

Introduction

The $Sn_2P_2S_6$ crystals are known as efficient photorefractive materials, that can be efficiently modified by their doping [1,2]. Our recent works are directed to a search for the new efficient dopants and their combinations, which are provided by two methods: growth in the presence of two types of impurities, and by the indiffusion of the metals (Cu, Ag) into previously grown samples [3]. In the communication, we present the results of the investigations of the optical and photorefractive parameters of the co-doped $Sn_2P_2S_6$:(Sb,Cu) crystals which demonstrate the best parameters.

Experiments

In course of our works, the various double-doped $Sn_2P_2S_6$ samples were grown using a conventional vapor-transport technique. We checked different combinations of the Sb (or Te), which, as were shown before [1,2], are the most efficient photorefractive dopants, with one of two metals, Ag and Cu, that were used for modification of the $Sn_2P_2S_6$ by the thermo-induced atom indiffusion [3]. It was founded that the most promising compound for photorefractive applications is the $Sn_2P_2S_6$ sample co-doped by a combination of Cu and Sb, with the equal concentrations of about 1 mol.%. Other dopant combinations, like Te+Cu, Te+Ag, and Sb+Ag, did not led to the enhancements of the photorefractive parameters, and demonstrated increased DC conductivity. So, the main attention was applied to the Sb+Cu co-doped crystals.

The measurements of the optical transmission spectra in these co-doped samples show that they are similar to the case of the Sb-doped $Sn_2P_2S_6$ crystals. The experiments on the photorefractive two-wave mixing were carried using He-Ne laser irradiation (633 nm). The measured max values of the two-wave mixing gain are Γ=15 cm^{-1} (at 1 um grating period and 0.3 $W{\cdot}cm^{-2}$ light beam intensity). The gain value depends on the light intensity and reduces down to 10 cm^{-1} at 0.1 $W{\cdot}cm^{-2}$, that is less as compared with the case of the $Sn_2P_2S_6$:Sb1% crystal [1,2]. But, the main advantage of the photorefractive effect in the $Sn_2P_2S_6$:(Sb,Cu) composition is the single-exponential dynamics of the photorefractive response when the formation of the space-charge grating occurs practically without the compensation processes that are usually observed in other doped (and double-doped) $Sn_2P_2S_6$ crystals. Also, the amplified signal demonstrates good stability, in comparison with the case of the Sb-doped $Sn_2P_2S_6$.

These Sb+Cu co-doped crystals, due to high enough two-wave mixing gain at 633 nm and temporal stability of the gain, allows realizing various photorefractive schemes on their base. This is illustrated by studying the performances of several optical schemes, namely: the dynamic interferometer based on the two-wave mixing, the ring-loop and the semi-linear oscillator scheme with high efficiency and low generation threshold compared with other doped photorefractive $Sn_2P_2S_6$ compounds.

Modelling

The obtained experimental results well correlate with our modelling performed by means of the *ab initio* calculations of the electron spectra in the $Sn_2P_2S_6$ lattice with various defects. The calculations provide an information about the energy of the defect levels in the gap, and also the most probable positions of the dopant that can be determined by minimization of the total energy of the cell at various defect positions. Also this model allows estimating the variations of the physical parameters of the crystal induced by the impurity.

The model calculation of the electron spectra in the $Sn_2P_2S_6$ lattice with two defects (Cu and Sb) in the same cell give an explanation of the absence of the compensations processes in the double-doped crystal. As it was shown by the photo-EPR studies [4], the Sb^{3+} impurity replaces the Sn^{2+} cations, and become charge-compensated due to appearance the Sn vacancies: $(3Sn^{2+} + 2V_{Sn}{}^{2-})^0$. This leads to formation the defects of two types, and can be a reason of the electron-hole compensation at the formation of the photorefractive holograms in the Sb-doped crystals. The Cu^{1+} impurity, located near Sb^{3+}, can compensate the appearance of the Sn vacancy. As it follows from the calculated electron spectra, the additional electron states originated from the Sb and Cu adatoms correspond to the same energy, and so are forming the single defect electron level in the gap. This correlates with the single-exponential dynamics of the space-charge grating formation, that is predicted by a single-level model of the photorefractive effect.

Conclusions

Thus, the co-doping of the $Sn_2P_2S_6$ crystals with Sb and Cu is a promising way to enhance their photorefractive parameters. This modification allows to obtain the photorefractive grating which is stable in time and does not demonstrate significant compensation processes.

References

[1] T. Bach, M. Jazbinšek, G. Montemezzani, P. Günter, A. Grabar, and Yu. Vysochanskii, J. Opt. Soc. Am. B 24, 1535 (2007).

[2] A. A. Grabar, M. Jazbinšek, A. N. Shumelyuk, Yu. M. Vysochanskii, G. Montemezzani and P. Günter. Photorefractive effects in $Sn_2P_2S_6$. In: "Photorefractive Materials and Their Applications II". Springer, New York 327 (2007).

[3] V. Shvalya, J. Zavašnik, V. Nasretdinova, H. Uršič, J. Kovač, A. Grabar, A. Kohutych, A. Molnar, D. R. Evans, D. D. Mihailović, U. Cvelbar, J. Mater. Chem. C 8, 9975 (2020).

[4] B. E. Kananen, E. M. Golden, S. A. Basun, D. R. Evans, A. A. Grabar, I. M. Stoika, W. McClory, N. C. Giles, L. E. Halliburton, Optical Materials Express 6(12), 3992 (2016).

Interferometric complex-field retrieval in photorefractive transient detection imaging

A. Esteban-Martín, Javier García-Monreal, Fernando Silva, Germán J. de Valcárcel

Departament d'Òptica i Optometria i Ciències de la Visió, Universitat de València,
Dr. Moliner 50, 46100-Burjassot, Spain

Introduction

A transient detection imaging system (TDI), also known as optical novelty filter, is an adaptive interferometric device that detects temporal changes in a scene while suppressing its static parts. Removal of background improves contrast and helps visualizing and measuring intensity and phase changes. Following the first proposal [1], most TDI systems are based on photorefractive two-wave mixing [2]. Previous works rely on conventional intensity measurements, where partial information about input signal phase changes is obtained by previous calibration using an input phase-output intensity transfer function of the particular system.

In this work, we report our results on the TDI output complex field, and its relation with the input signal phase changes, via photorefractive two-wave mixing in a strontium-barium niobate (SBN) crystal. The single-frequency laser beam @532nm is split into a signal beam, a pump beam, and a reference beam for interferometry. Signal and pump beams intersect at the SBN crystal, whose c^+-axis is oriented to get virtually complete signal depletion under steady-state operation: the signal output port is a dark port. Any modification from that state produces a signal output so changes are revealed with high contrast.

To illustrate the phase performance of the device, the input signal beam is reflected onto a piezo-mirror for fine control of phase changes. Output signal phase is retrieved from off-axis Fourier holography which, compared to conventional intensity-based TDI, provides important additional features such as directionality of the phase change, higher resolution, and differential-phase measurement for enhanced sensitivity, all this without calibration.

We have evidenced the linear relation between input ($\Delta\varphi_1$) and output ($\Delta\varphi_{\text{out}}$) phase changes for the entire range from $-\pi$ to π (see Fig. 1) in excellent agreement with our theory [3],

$$\Delta\varphi_{\text{out}} = \frac{1}{2}\left(\Delta\varphi_1 + \pi\,\text{sign}\,\Delta\varphi_1\right), \tag{1}$$

which predicts a π jump "amplification" around $\Delta\varphi_1 = 0$.

Here we report new results on TDI for dynamic microscopic phase objects. We have modified the original setup [3] with a microscope objective and tube lens, achieving imaging resolutions around 1 μm, and phase target objects mounted on motorized translation stages. With this setup, we investigate interferometric transient phase retrieval of moving objects (see Fig. 2).

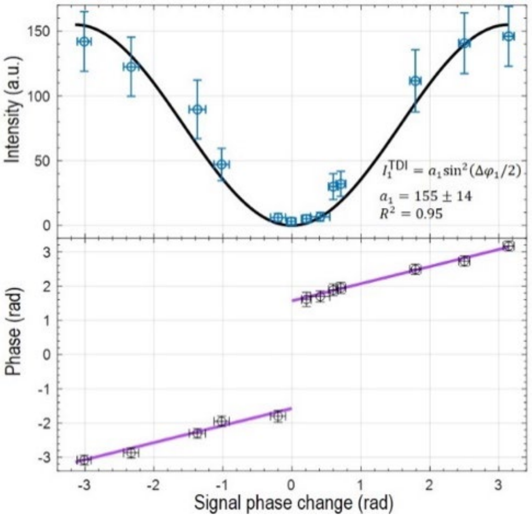

Fig. 1. Transient output intensity (top) and phase (bottom) depending on the applied signal-phase change. Intensity is fitted whereas phase follows the linear theoretical Eq. (1).

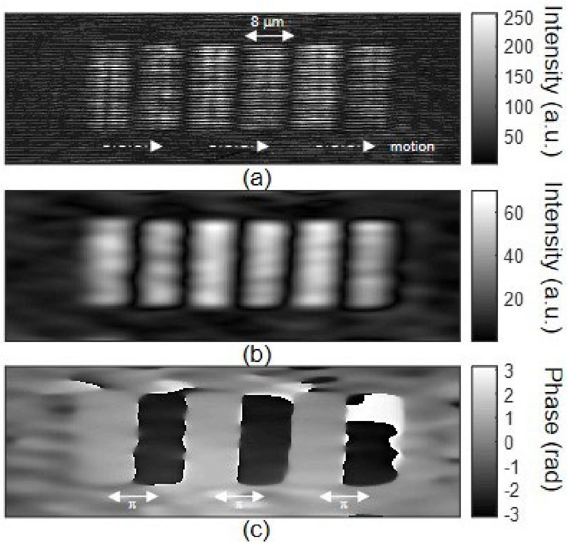

Fig. 2. Example of transient 2D interferogram (a), and retrieved intensity (b) and phase (c) of 3 rectangular phase objects moving from left to right. Differential phase shows π "amplification".

Conclusions

We have demonstrated photorefractive TDI with interferometric complex-field retrieval.

We have evidenced the linear relation existing between input and output phase changes for the entire range from −π to π in agreement with our theory.

Phase-change inference from transient phase (complex field) measurements improves inference from transient intensity measurements, reaching /30 resolution without pre-calibration.

We have demonstrated differential-phase detection in TDI, showing the direct measurement of phase changes, and π jump "amplification" around zero.

Finally, we believe that this work takes advantage of adaptive background suppression with high phase-sign sensitivity, especially important for low-power small-phase change signals sensors, and opens up new possibilities for imaging and temporal single-spot signal detection [4].

References

[1] R. S. Cudney, R. M. Pierce, and J. Feinberg, "The transient detection microscope," Nature **332**, 424–426 (1988).

[2] M. Woerdemann, F. Holtmann, and C. Denz, "Full-field particle velocimetry with a photorefractive optical novelty filter," Appl. Phys. Lett. **93**, 021108 (2008).

[3] A. Esteban-Martín, J. García-Monreal, F. Silva, and G. J. de Valcárcel, "Interferometric measurement of complex-field changes in transient detection imaging, " Optics Express **28**, 28782–28791(2020).

[4] K. Shcherbin and M. B. Klein, "Adaptive interferometers with no external field using reflection gratings in CdTe:Ge at 1550 nm," Opt. Commun. **282**, 2580–2585 (2009).

We acknowledge financial support from the Spanish Government through projects PID2020-120056GB-C21 and PID2020-120056GB-C22 funded by MCIN/AEI/ 10.13039/501100011033.

Learning in Holographic Convolutional Neural Nets

Kelvin Wagner
Optoelectronic Computing Systems Center, Dept of ECEE, University of Colorado, Boulder, CO, USA

Abstract: We show how the array of convolutional adaptive interconnections needed for deep learning can be physically implemented and learned in an all-optical multistage dynamic holographically-interconnected architecture using thick Fourier-plane dynamic holographic photorefractive crystals. This optical architecture is self-aligned, phase-calibrated, and aberration compensated by using photorefractive phase-conjugate mirrors to record the dynamic-holographic Fourier-plane interconnections in each layer.

Van Heerden introduced the metaphorical connection between neural computation and volume holography nearly 60 years ago. [1] A variety of holographic interconnection approaches to building optical neural networks were investigated in the 80s and 90s. [2–4] Since these planar technologies have the same component density scaling as 2-D electronic neural networks numerous optical researchers instead investigated the use of 3-D photorefractive (PR) crystals for neural-network weighted interconnections. PR crystals were used both as nonlinear dynamical systems with emergent neural computational capabilities [5–7] as well as the weighted adaptive holographic interconnections in optical neural networks. [8, 9] These 3-D volume-holographic interconnections have a potential for a dramatically larger interconnection weights storage capacity ($10^{11}/\mathrm{cm}^3$) than planar integrated-electronic or integrated-optical approaches. These adaptive holographic systems can be made to self align by using phase-conjugate mirrors. [10–12] Multi-layer optical networks using cascaded holograms and trained by back propagation were also investigated. [13–17] The critical missing ingredient in developing an all-optical multi-layer adaptive neural network is a practical nonlinear neuron. Recent quantum optic and integrated-photonic programmable activation function demonstrations have shown capability for a variety of flexible nonlinearities and indicated capability for digitally controlled or simulated learning. [18–21] But none of these approaches have addressed the critical requirement for appropriate bidirectional gradient operation through the nonlinearity needed for backwards error propagation, so we introduce in Fig. 1 a novel bidirectional optical ReLU (Rectifying Linear Unit), [22] the modern nonlinear neuron activation function that enables deep learning by avoiding the sigmoidb derivative blocking of back propagation errors from penetrating deep into the trainable multi-layer network.

Various approaches to a front-end convolutional layer and optical convolutional neural networks (CNNs) have been proposed and demonstrated as single layers or in simulations, [21, 23, 24] but have not addressed the key components of modern deep learning CNNs including multiple feature planes, variable template sizes, pooling and resolution decrease, and back propagation learning of the shared weights that we incorporate. [22] Adjoint method training using concepts of numerical phase conjugation has been developed for neural network and integrated optics optimization but without an appropriate differentiable nonlinearity multiple layers and convolutional operation has not been achieved. [25] An integrated-photonic approach utilizing a thin-film photorefractive adaptive holographically-interconnected vector-matrix-multiplier is being developed [26], but so far only single layers without back propagation, with a limit of about a million weights, and without the capability for multiple convolutional feature planes. We instead exploit the massive parallelism of bulk photorefractive holographic optical systems with the potential for billions of adaptive weights per layer (corresponding to 10^{11} convolutional multiply-and-adds per layer with scores of input and output feature planes). This approach is based on deep learning in a multi-layer architecture consisting of spatially-multiplexed arrays of optical rectifying neurons convolutionally interconnected by arrays of adaptive Fourier-holographic weights as in Figs. 2 and 3. By using photorefractive phase-conjugate mirrors for the adaptive holographic recording, this system avoids problems with alignment, aberrations, and device imperfections. The optical ReLU device enables practical, low-power, multi-layer

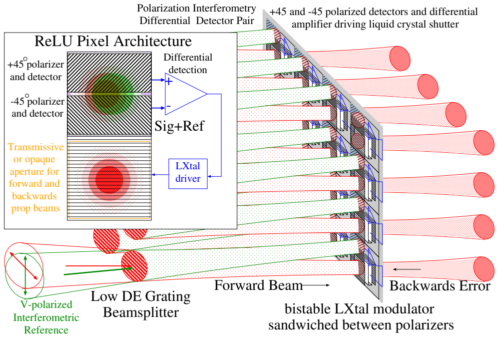

Figure 1: Bidirection optical ReLUs using polarization interferometry in an LCoS smart-pixel array geometry.

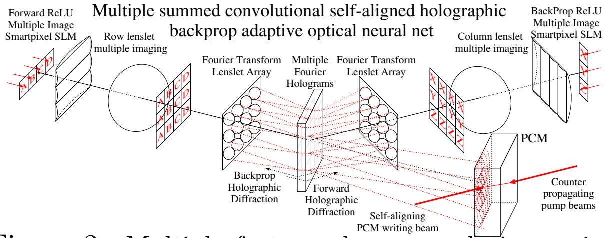

Figure 2: Multiple feature plane convolutions using lenslets and self-aligning Fourier volume hologram.

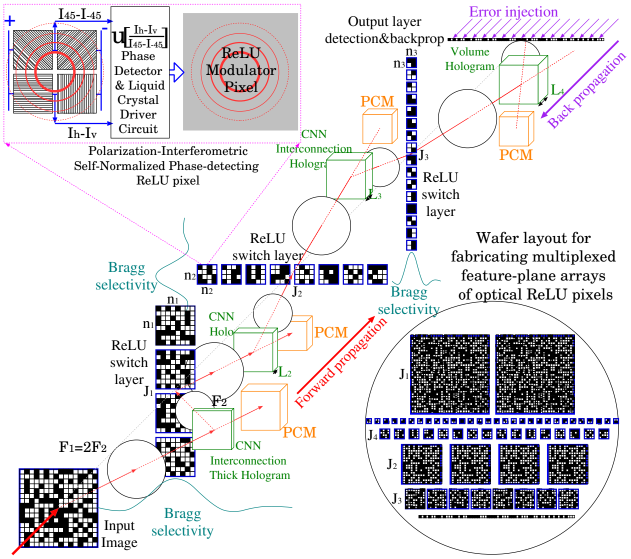

Figure 3: Multiple layers of self-aligning, angular-multiplexed, convolutional Fourier holograms using optical ReLU neuron layers and PR crystal interconnects.

neural-network cascades while enabling fully-reciprocal bidirectional operation for back propagation based adaptive holographic learning. When built, this system will be capable of achieving a competitive computational throughput to special purpose deep learning supercomputers with only moderate speed neurons and slowly evolving photorefractive interconnection convolutional feature plane weights.

References

[1] P. J. van Heerden, "Optical information storage in solids," *App. Opt.*, vol. 2, p. 393, 1963.
[2] E. G. Paek et al, "Optical associative memory using FT holograms," *Opt. Eng.*, vol. 26, p. 428, 1987.
[3] D. Psaltis et al, "Holography in artificial neural networks," *Nature*, vol. 343, p. 325, 1990.
[4] A.V. Pavlov et al, "Holographic correlators and optical neural networks," *J Opt Tech*, vol. 61, p. 42, 1994.
[5] D.Z. Anderson et al, "Resonator memories and optical novelty filters," *Opt. Eng.*, vol. 26(5), p. 434, 1987.
[6] Y. Owechko, "Optoelectronic resonator neural networks," *App. Opt.*, vol. 26(23), p. 5104, 1987.
[7] D. Anderson, "Information dynamics of photorefractiove two-beam coupling," *PRL*, vol. 82, p. 1418, 1999.
[8] D.Psaltis, D.Brady, K.Wagner, "Adaptive optical networks using PR Xtals," *AO*, vol. 27, p. 1752, 1988.
[9] K. Wagner, "Optical Competitive Learning With LXtal WTA Modulators," *AO*, vol. 32, p. 1408, 1993.
[10] B.H. Soffer et al, "Associative holographic memory with feedback using PCM," *Opt. Lett.*, vol. 11(2), 1986.
[11] Y. Owechko, "Optical interconnection for neural networks using SP-PCM," *Opt. Let.*, vol. 16, p. 675, 1991.
[12] I.M. Beldyugin et al, "Optical neurocomputers based on PR Xtals," *Kvan. Elek.*, vol. 19, p. 424, 1992.
[13] K. Wagner and D. Psaltis, "Multilayer optical learning networks," *Appl. Opt.*, vol. 26, p. 5061, 1987.
[14] I. Saxena et al, "Adaptive multilayer optical neural-network," *Opt. Eng.*, vol. 34, p. 2435, 1995.
[15] D. Psaltis and Y. Qiao, "Adaptive multilayer optical networks," *Prog. Opt.*, vol. 31, p. 227, 1993.
[16] Y. Owechko, "Cascaded-grating holography for artificial neural nets," *App. Opt.*, vol. 32, p. 1380, 1993.
[17] G. C. Petrisor, "Backward-error-propagation learning in PR crystals," *App. Opt.*, vol. 35, p. 1328, 1996.
[18] A. Ryou et al, "Free-space optical NN based on atomic nonlinearity," *Phot Res*, vol. 9(4), p. B128, 2021.
[19] I. Williamson et al, "Reprogrammable EO Nonlinear Activation Functions," *IEEE JSTQE*, vol. 26, 2020.
[20] M. Frad, "Experimental realization of arbitrary activation functions ," *Opt Exp*, vol. 28, p. 12138, 2020.
[21] N. Passalis et al, "Training Photonic CNN With Sinusoidal Act.," *IEEE T Comp Intel*, vol. 5, p. 384, 2021.
[22] K. Wagner, "Optical ReLUs for Back-Prop Learning in Deep Holographic CNN," *IEEE JSTQE v26*, .2020
[23] S. Colburn, "Optical frontend for a convolutions neural network," *App. Opt.*, vol. 58(12), p. 3179, 2019.
[24] B. Muminov et al, "Fourier optical preprocessing in lieu of deep learning," *Optica*, vol. 7(9), p. 1079, 2020.
[25] T. Hughes, "Training of photonic NN through in situ backpropagation ," *Optica*, vol. 5(7), p. 864, 2018.
[26] R. Dangel et al, "Integrated photonic synaptic interconnect processor," in *APC*, p. IM2A.1, OSA, 2020.

Light and thermally-induced charge transfer phenomena at ferroelectric crystal surfaces

Carlos Sebastián-Vicente,[1] Ángel García-Cabañes,[1,2] Mercedes Carrascosa[1,2]

[1]Departamento de Física de Materiales, Universidad Autónoma de Madrid, 28049 Madrid, Spain
[2]Instituto Nicolás Cabrera, Universidad Autónoma de Madrid, 28049 Madrid, Spain

Lately, evanescent electric fields generated by the bulk photovoltaic (PV) effect and the pyroelectric (PY) effect have attracted significant interest for multiple applications (particle/droplet manipulation and trapping [1-4], droplet dispensing [5-6], electro-wetting [3], orientation of liquid crystals [7], etc). In this context, the ferroelectric surface plays a key role, and we have discovered a new interaction mechanism when ferroelectrics come into contact with other objects, exploiting the PV and PY effects. On one hand, in this work we present experimental evidence of charge transfer between ferroelectric crystals and micro/nanoparticles in contact with their surface, driven by optical or thermal stimuli [2, 8]. On the other hand, we have taken this new mechanism one step further and demonstrated the feasibility of transferring PV/PY-induced surface charge patterns to passive dielectric substrates.

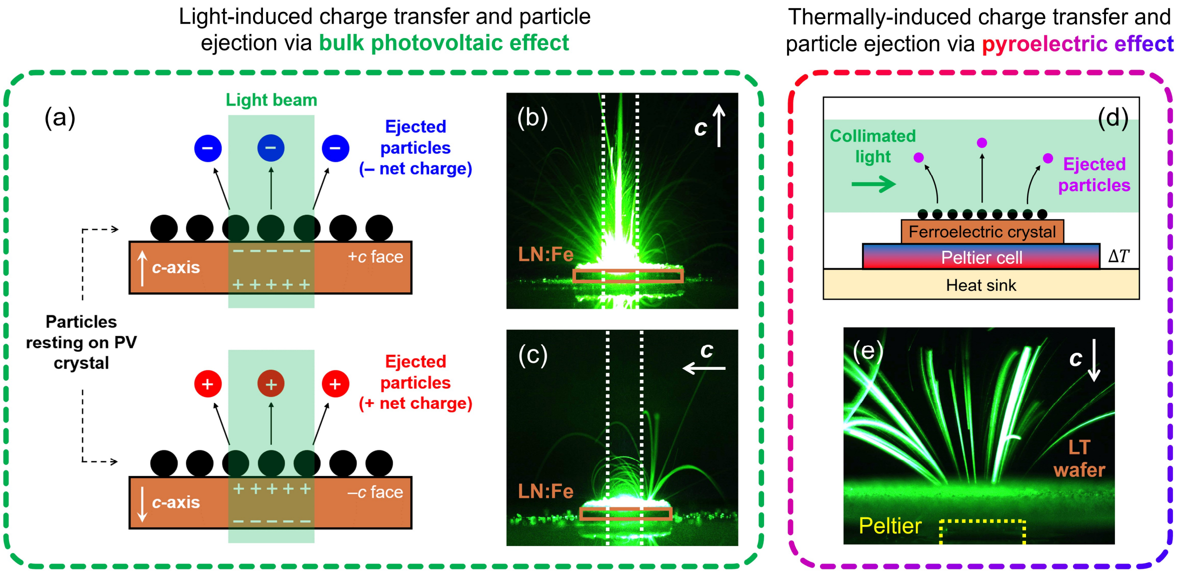

Figure 1: a) Illustration of the charge transfer and ejection of particles from z-cut ferroelectric PV crystals triggered by light excitation. Images b) and c) show the ejection of Al_2O_3/ $CaCO_3$ microparticles from z-cut/ x-cut $LiNbO_3$:Fe, respectively. The white dotted lines indicate the position and diameter (3 mm) of the light beam ($\lambda = 532$ nm, $I = 86$ mW/cm^2). d) Experimental configuration for observing thermally-driven ejection of particles from ferroelectric surfaces. e) Ejection of $CaCO_3$ microparticles from z-cut $LiTaO_3$ upon local cooling ($\Delta T \approx -16$ °C, Peltier area: 9×9 mm^2).

Regarding the first aspect, i.e. charge transfer to micro/nanoparticles, we have thoroughly studied the influence of the type of particle (metallic or dielectric), crystal orientation, light intensity, wavelength and surrounding medium. Furthermore, although most experiments have been conducted with LiNbO$_3$:Fe (LN:Fe) crystals, we have also tested the effect in other ferroelectrics (such as LiTaO$_3$), thanks to the generality of the PY effect. In Figure 1 we summarize our results.

More recently, we have also investigated the feasibility of another kind of charge transfer, from the ferroelectric surface to a passive dielectric substrate, and even the possibility of transferring micrometric charge patterns. The proposed procedure is simple and resembles the operation of a stamp: upon contact, part of the PV/PY charge generated in the ferroelectric is transferred and stored at the surface of the dielectric substrate. The method has been successfully applied with glass, quartz and PMMA passive substrates, and the transferred charge patterns have been exploited to massively trap and pattern nanoparticles. A representative result is shown in Figure 2. A very similar particle distribution can be observed on the active ferroelectric crystal and the passive dielectric substrate, indicating a successful charge transfer that keeps the original pattern generated at the ferroelectric surface. Moreover, from a practical point of view, the results show the possibility for nanoparticle trapping and patterning in common passive substrates instead of LN:Fe.

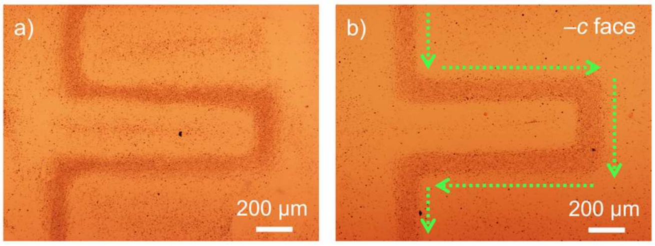

Figure 2: a) Pattern of Ag nanoparticles on a quartz substrate after contacting a *z*-cut LN:Fe crystal illuminated with a scanning Gaussian beam ($\lambda = 532$ nm, $1/e^2$ diameter of 150 µm, , intensity $I =$ 29 W/cm^2, average speed of around 50 µm/s). b) Counterpart directly on the *z*-cut LN:Fe substrate illuminated with the same light pattern. The trajectory of the laser beam is indicated by green dotted arrows.

Overall, different charge transfer phenomena from the ferroelectric surface are reported here, which open the way towards novel functionalities and applications of ferroelectric platforms.

Funding from the Ministerio de Economía, Industria y Competitividad (MAT2017-83951-R) and the Ministerio de Ciencia e Innovación of Spain (PID2020-116192RB-I00) is gratefully acknowledged.

References

[1] M. Carrascosa et al., Appl. Phys. Rev. **2**, 040605 (2015)
[2] C. Sebastián-Vicente et al., Part. Part. Syst. Charact. **36**, 1900233 (2019)
[3] B. Fan et al., Phys. Rev. Appl. **7**, 064010 (2017)
[4] A. Zaltron et al., Adv. Mater. Interfaces, 2200345 (2022)
[5] P. Ferraro et al., Nat. Nanotechnol. **5**, 429 (2010)
[6] A. Puerto et al., Adv. Mater. Interfaces **8**, 2101164 (2021)
[7] L. Lucchetti et al., Opt. Mater. **73**, 64 (2017)
[8] C. Sebastián-Vicente et al., Adv. Electron. Mater. **8**, 2100761 (2022)

Light-shaped virtual electrodes on Fe:LiNbO$_3$ to control confined droplets

Riccardo Zamboni,[1] Jörg Imbrock,[1] Cornelia Denz[1]

[1]Institute of Applied Physics, University of Münster (WWU)
Corrensstr. 2/4, 48149 Münster, Germany

Introduction

Reliable manipulation of microfluidic droplets is needed for efficient miniaturization of chemical and biological assays [1], as well as for the synthesis of new materials [2] using droplets as units in complex protocols within portable devices. Light-based techniques offer the utmost flexibility due to the advanced technologies for sculpting and shaping light [3]. A wide range of optical methods were investigated to control droplets, such as by mechanical actuation [4], optical trapping [5], photophoresis [6], photopyrophoresis [7], and light-induced dielectrophoresis [8]. Among these techniques, light-shaped virtual electrodes are the most promising for the unlimited control of the electric field configurations. Such a feature is, indeed, highly demanded in the new generation of lab-on-a-chip[10], which aims to integrate multiple operations on different droplets into the same platform.

The photo-induction of virtual electrodes requires a layer within the device capable to convert the light stimuli into charge distribution (e.g. photoconductive, or photopyroelectric). The most exploited material for the generation of electric fields for droplet manipulation (i.e. several kV mm^{-1}) is iron-doped lithium niobate (Fe:LiNbO$_3$). This ferroelectric crystal enabled the light-induced manipulation of microfluidic droplets using virtual electrodes, either generated by its bulk photovoltaic effect [9] or by the optothermally actuated pyroelectric effect [7].

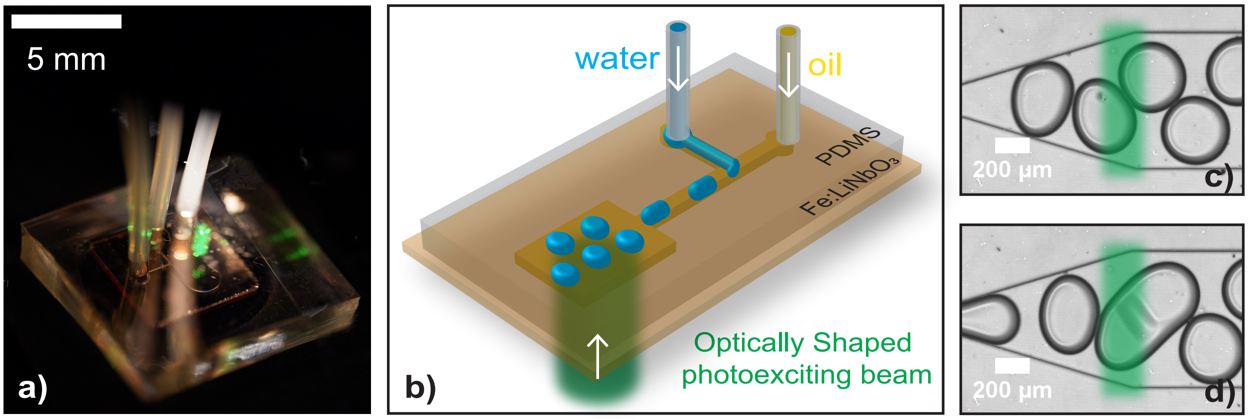

Figure 1: The image in a) shows the device during the exposure of the virtual electrodes with green light from a cw laser. PDMS and Fe:LiNbO$_3$ are the two layers of the devices, shown in the sketch in b). The green light is optically shaped by an amplitude spatial light modulator (Holoeye) in a 4f lens configuration. A 240 µm wide stripe enabled the droplets merging, as shown by two images captured before c) and after d) the exposure of the pattern, respectively.

In this contribution, we present virtual electrodes on Fe:LiNbO$_3$ for the manipulation of confined aqueous droplets (See the device in Fig. 1a)). As in a typical lab-on-a-chip, the droplets flow in a channel with a cross-section smaller than the radius of unconfined ones. As shown in the sketch in Fig. 1b), a layer of Polydimethylsiloxane (PDMS) contains the microfluidic channels, consisting of a T-junction to produce water droplets immersed in an insulating oil medium. The droplets interact with the electric field photoinduced on a 0.5 mm thick Fe:LiNbO$_3$ (Altechna) with an iron concentration of 0.1% mol. Either droplet merging or trajectories are achieved using stripe-shaped light-induced virtual electrodes on the ferroelectric layer. Fig. 1c) and 1d) show an example of two droplets merging right after the exposure of the crystal with a stripe pattern. The number of droplets merged and the speed of the phenomena are proportional to the strip width and light intensity. Similarly, the trajectories of a single droplet can be designed by the shape of the virtual electrodes and the light intensity of the pattern used during the exposure time. Notably, droplet merging presented two different behaviors at two timescales. For exposures in the range of milliseconds, two droplets merge as shown in Fig. 1c), while in the range of seconds the whole emulsions broke into a single larger droplet.

Conclusions

This contribution aims to demonstrate the introduction of light-induced virtual electrodes for the manipulation of aqueous droplets confined in microfluidic channels using a Fe:LiNbO$_3$ crystal. Optical shaping techniques were used to define stripe-shaped virtual electrodes within this platform for droplet manipulation, either for on-demand droplet merging, or controlling droplet trajectories.

The integration of this material in lab-on-a-chip devices may satisfy the demand for the introduction of a reconfigurable droplet manipulation tool. In addition, lab-on-a-chips can benefit from the exploitation of other recent development of this material for this type of application such as an optically integrated system [11] or its biocompatibility [12].

References

[1] W. Feng, E. Ueda, Erica, P. A. Levkin, Advanced Materials **30**, 1706111 (2018)

[2] H. Cui, X. Wang, J. Wesslowski, T. Tronser, J. Rosenbauer, A. Schug, G.Davidson, A. A. Popova, P. A. Levkin, Advanced Materials **33**, 2006434 (2021)

[3] K.Dholakia, T. Čižmár, Nature **5**, 335-342 (2011)

[4] J. LV, Y. Liu, J. Wei, E. Chen, L. Qin, Y. Yu, Nature **537**, 179-184 (2016)

[5] M. Esseling, C. Alpmann, J. Schnelle, R. Meissner, C. Denz, Scientific Reports **8**, 5029 (2018)

[6] M. Esseling, P. Rose, C. Alpmann, C. Denz, Applied Physics Letter **101**, 131115 (2012)

[7] W. Li, X. Tang, L. Wang, Science Advances **6**, eabc1693 (2020)

[8] M. Esseling, A. Zaltron, W. Horn, C. Denz, Laser & Photonics Reviews **9**, 98-104 (2015)

[9] P. Andrés, A. Méndez, L. Arizmendi, A. García-Cabañes, M. Carrascosa, Phyics Review Applied, **14**, 024046 (2020)

[10] F. Paratore, V. Bacheva, M. Bercovici, G. V. Kaigala, Nature Reviews Chemistry **6**, 70-80 (2022)

[11] R. Zamboni, A. Zaltron, M. Chauvet, C. Sada, Scientific Reports **11**, 17987 (2021)

[12] L. Miccio, J. Behal, M. Mugnano, P. Memmolo, B. Mandracchia, F. Merola, S. Grilli, P. Ferraro, ACS Applied Bio Materials **2**, 4675–4680 (2019)

MgO-LiNbO$_3$ films: an appealing photorefractive medium

Mathieu Chauvet[1], Anton Perin[2], Ludovic Gauthier-Manuel[1]

[1] *FEMTO-ST institute, UMR CNRS 6174, University of Bourgogne Franche-Comté, 15B Avenue des Montboucons, 25030 Besançon, France*
[2] *Tomsk State University of Control Systems and Radioelectronics (TUSUR), 40, prospect Lenina, 634050, Tomsk, Russia*

Introduction

LiNbO$_3$ films (LNF) are presently at the heart of an intense research activity due to a strong potential for RF components, exploiting piezoelectric properties, and for the development of integrated optical chips, using electro-optical and nonlinear properties [1-3]. This material is also known as a holographic medium due to its photorefractive (PR) properties [4] which has been mainly studied and exploited in bulk crystals but several reasons motivate the study of the photosensitivity of LNF.

First of all, PR performance such as sensitivity and response time can be improved thanks to a slab geometry. Moreover, the interaction between beams is facilitated due to the 1-D light confinement. In addition, new architectures are possible such as the control of guided beams using external beams. Finally, the potential applications are enlarged with the possibility of integrating photonic and electronic components in the case of LNF on silicon substrate.

LNF considered in this work are fabricated from photonic grade 500µm thick LiNbO$_3$ wafers doped with 5%mol of magnesium oxide (MgO). A buffer layer of silica (typically 1 µm) is first deposited onto one face of the wafer followed by the sputtering of a typical 200 nm gold layer. A similar gold layer is then deposited on a high flatness silicon wafer. Both wafers are then placed into contact and pressed to form a strongly gold bonding. The bonding process is realized at room temperature in order to avoid mechanical stresses due to the different thermal coefficients of silicon and LiNbO$_3$. Finally, the formed heterostructure is ground and polished to give a slab waveguide consisting of a 7µm thick LNF on a silicon substrate with a silica and gold buffer layers. This hybrid wafer is cut using a precision saw to form rectangular samples with polished faces.

The PR properties of such planar waveguides are then analyzed using a 532nm CW beam of about 15µm diameter (FWHM) injected by the saw-cut faces. The samples temperature can be modified and stabilized using a Peltier module in order to induce a homogeneous pyroelectric field inside the sample [4]. In presence of an adequate PR effect, the beam self-confines laterally and gives rise to propagation without diffraction, a solitonic regime can thus be reached [5, 6]. It is important to note that the LNF used in the present study is doped with MgO which is known to avoid the PR effect so that stable operation can be obtain for photonic components (modulator, frequency converters, …) made out of LiNbO$_3$.

The experiment carried out here shows to the contrary that an efficient self-focusing takes place for low power beams giving rise to soliton beams. As an illustration, figure 1 shows that an injected beam of 60 µW self-focusses in less than 300ms when the temperature of the structure is raised 5°C above room temperature. Few microwatts power beam can self-trap in few seconds as revealed by the second measurement. The analysis confirms that the response time decreases inversely proportional to the injected power, which allows us to deduce that light power of a few mW would give a response time near a few ms. Furthermore, it should be noted that this efficient self-focusing induces a memorized 2-D waveguide in the material. This can thus be used as a reconfigurable waveguide to transmit a signal at a wavelength for which the photosensitivity is negligible as in the near IR.

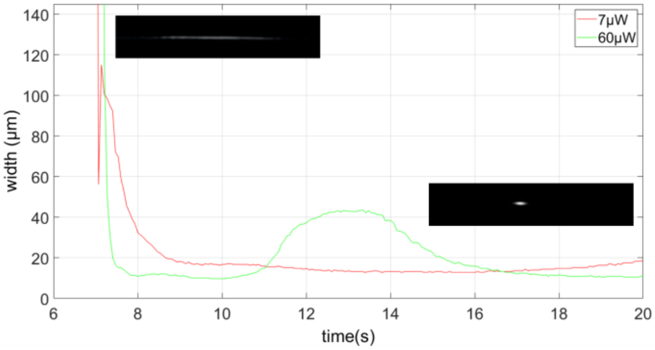

Figure 1: Transverse beam width evolution observed at the output face of a 2 cms long LNF:MgO for two different beam power. Insert corresponds to output images of at two characteristic time (initial and best focusing).

Conclusions

This surprising high photosensitivity combined with response times which are at least two orders of magnitude lower than the responses in bulk undoped $LiNbO_3$ opens the way to the realization of reconfigurable structures in MgO:LNF. The underlying physics along with a detailed description of the dynamics and potential applications will be presented in details.

References

[1] J. Lu et.al, “ultralow-threshold thin-film lithium niobate optical parametric oscillator”, Optica **8**, 539-544 (2021).
[2] V. Pêcheur et. al., “Watt-level SHG in undoped high step-index PPLN ridge waveguides”, OSA continuum, 4, 1404-1414, (2021).
[3] M. Zhang et. al., “Integrated lithium niobate electro-optic modulators : when performances meets scalability”, optica **8**, 652-667 (2021)
[4] A.M. Glass et.al., “Highvoltage bulk photovoltaic effect and the photorefractive process in LiNbO3”, Applied Physics Letters, **25**, 233-235, (1974)
[5] J. Safioui, F. Devaux, and M. Chauvet, “ Pyroliton: pyroelectric spatial soliton ”, Opt. Express **17**, 22209, (2009)
[6] M. Chauvet et. al., “Fast-beam self-trapping in LiNbO3 films by pyroelectric effect”, Optics Letters, 40, 1258-1261 (2015).

Optical response of strained $LiNbO_3$ crystals from first principles

Mike Nico Pionteck[1] and Simone Sanna[1]

[1]Institut für Theoretische Physik and Center for Materials Research (LaMa), Justus-Liebig-Universität Gießen, Heinrich-Buff-Ring 16, 35392 Gießen, Germany

Introduction

The investigation of optical response study has become a widely used non-destructive method to characterize crystalline solids and nanostructures. X-ray diffraction measurements have shown that domain walls in lithium niobate (LN) behave like compressed bulk material [1]. Therefore, studying the optical response of LN as a function of compression may help to understand the optical response of the domain walls of LN. For this purpose, we have calculated the optical susceptibility, including second harmonic (SHG) and third harmonic generation (THG), of strained LN from first principles.

Methodology

In order to model strained LN, we have done calculations within density functional theory (DFT) as implemented in VASP [2]. For the exchange-correlation functional, the formulation of PBE [3] has been used. In a first approximation, compression was modeled by decreasing the lattice constants of the orthorhombic unit cell in x-, y- and z-direction, respectively, and minimizing the Hellmann-Feynman forces. This has been done in steps of 0.8 % up to 2.4 % with respect to the lattice constant.

The optical response has been calculated using time-dependent DFT (TDDFT) as implemented in Yambo [4]. The Bloch wave functions are calculated with QuantumEspresso using an $8 \times 5 \times 3$ k-point mesh, which corresponds to 61 irreducible k-points. A Kohn-Sham basis set consisting of the 100 highest valence bands and 100 lowest conduction bands has been considered for the calculation of the time-evolution of the dynamical polarization in Yambo.

Results

Our calculations reveal that structural strain strongly affects all the components of the second- and third-order polarizability tensor χ^2 and χ^3. Changes of the intensities and frequency shifts of the optical signatures occur. For instance, our calculations predict a roughly linearly increasing intensity for the $|\chi^2_{zzz}|$ component, as can be seen in Fig. 1 (a).

Due to the threefold rotational symmetry, unstrained LN has four independent χ^2 elements [5]. In contrast, when compressed in x- and y-direction, the degeneracy of some identical χ^2 components is lifted, as shown by our calculations. In particular, $|\chi^2_{yyy}|$ and $|\chi^2_{yxx}|$, which match in unstrained LN, split strongly upon compression in x-direction, as displayed in Fig. 1 (b) for a wavelength of 1035.90 nm. As shown in Fig.1 (b), $|\chi^2_{zyy}|$ and $|\chi^2_{zxx}|$ are also split upon compression in x-direction.

In addition, linear optical properties such as the refractive index as well as the birefringence are obtained from the calculated dielectric tensor as a function of compression. For instance, the birefringence for a wavelength of 1035.90 nm in dependence on compression in z-direction is shown in Fig. 1 (c). As can be seen, the birefringence is linearly decreasing with compression in z-direction.

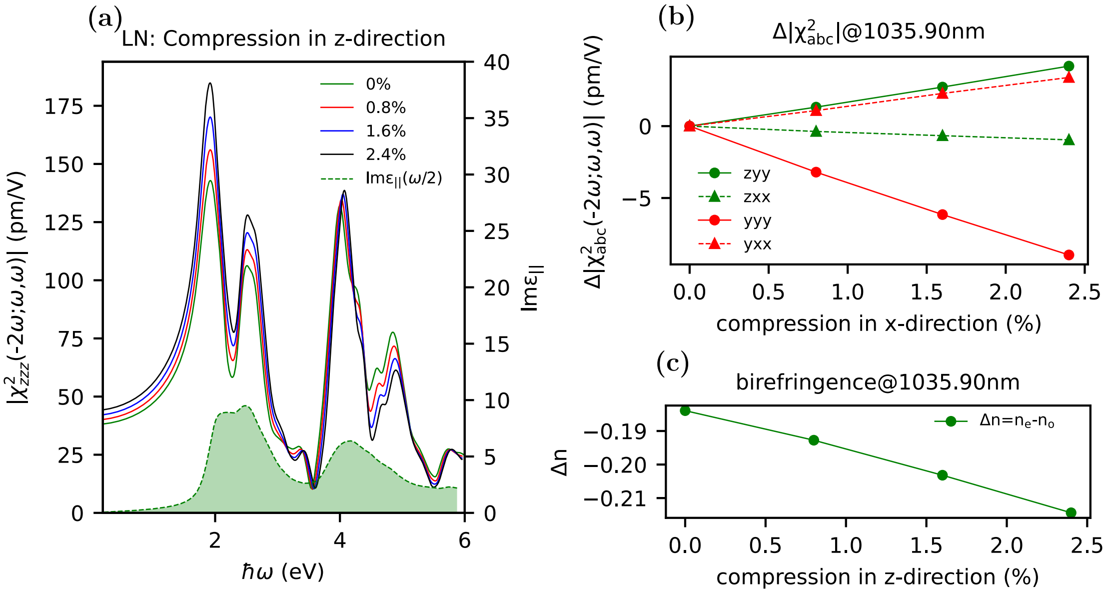

Figure 1: (a) The calculated SHG spectra of $|\chi^2_{zzz}|$ and the imaginary part of the extraordinary dielectric function of LN compressed in z-direction. (b) The relative change of the calculated intensity of $|\chi^2_{yyy}|$, $|\chi^2_{yxx}|$, $|\chi^2_{zyy}|$ and $|\chi^2_{zxx}|$ for a wavelength of 1035.90 nm of LN for compression in z-direction. (c) The calculated birefringence for a wavelength of 1035.90 nm of LN for compression in z-direction.

Conclusions

Both SHG and THG spectra of unstrained and strained LN are obtained from our calculations. Changes in the intensity and frequency shifts are yielded for all components. Due to symmetry reduction, identical χ^2components are lifted for compression in x- and y-direction. Our results may help to understand the optical response of domain walls in LN. Additionally, knowledge of the refractive index and birefringence is important for applications such as Ti waveguides.

References

[1] M. Rüsing *et al.*, Phys. Rev. Mat. **2**, 103801 (2018)
[2] G. Kresse and J. Furthmüller, Phys. Rev. B **54**, 11169 (1996)
[3] J. Perdew *et al.*, Phys. Rev. Lett. **78**, 1396 (1997)
[4] C. Attaccalite and M. Grüning, Phys. Rev. B **88**, 235113 (2013)
[5] A. Riefer *et al.*, Phys. Rev. B **87**, 195208 (2013)

Optical response of the newly discovered hexagonal phase of Ta2O5 (calculated) from first principles

Christa Fink [1], Felix Bernhardt [1], Giulio Favaro [2], Marco Bazzan [2], Simone Sanna [1]

[1] Institute for Theoretical Physics, Univ. of Giessen,
Heinrich-Buff-Ring 16, 35392 Giessen, Germany
[2] Department of Physics and Astronomy, Univ. of Padua, Italy

Introduction

Ta_2O_5 is known as a relatively chemically inert material with high density and high refractive index. It has low absorption coefficients from near-UV to near-IR and is therefore usually employed in optical coatings, e.g. for mirror coatings in gravitational-wave detectors. One of the main problems gravitational-wave interferometer coatings face is the Brownian thermal noise which is always present at non-zero temperature. In the case of amorphous materials used for these coatings this problem is also coupled with a requirement of very low optical absorption. The main idea therefore is to partially crystallize these coatings to reduce Brownian noise without introducing too much unwanted optical effects like scattering.

Experimental studies of thermically produced nanocrystals in amorphous Ta_2O_5 thin films indicate a new crystalline phase of Ta_2O_5. These crystals were characterized by Grazing Incidence X-Ray Diffraction (GIXRD). The phase has a hexagonal structure with cell parameters of around 7.2 Å and 3.8 Å.

Theoretical investigations

This new phase is modeled from first principles in the framework of the Density Functional Theory (DFT) as implemented in VASP [1, 2]. In this work we present, besides the ground state structural properties, the optical response of the newly proposed hexagonal Ta_2O_5 phase. The optical properties are calculated with different approaches of different precision, ranging from the independent particle approximation to the GW-approach (many body perturbation theory). Additionally, we compare the optical responses of the new hexagonal phase with those of known phases of Ta_2O_5, e.g. the orthorhombic and monoclinic phases.

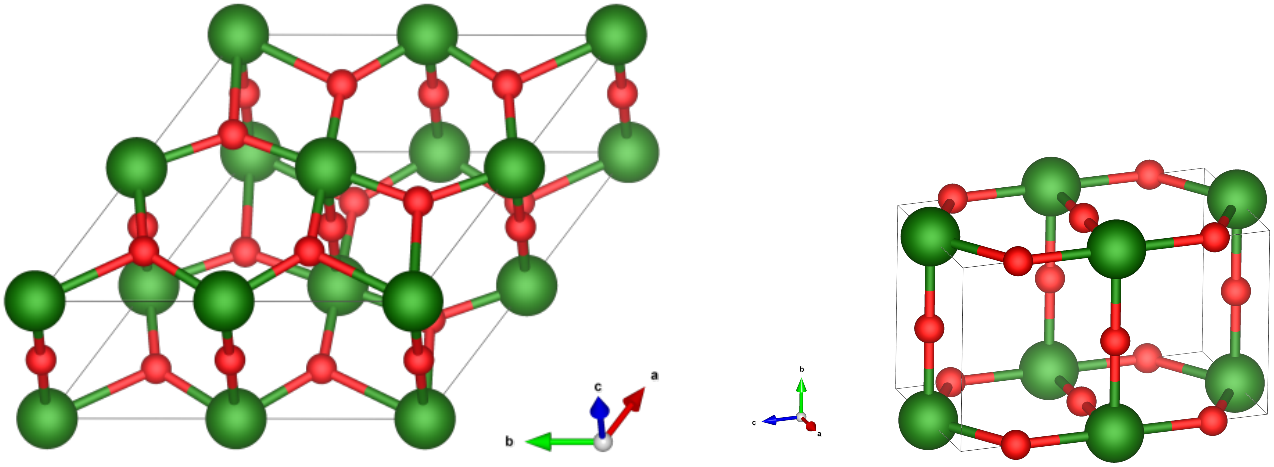

Figure 1: *Left*: Atomic structure of hexagonal δ-Ta_2O_5. The unit cell includes 4 atoms of Tantalum (green) and 10 atoms of Oxygen (red). *Right*: Atomic structure of simplified orthorhombic Ta_2O_5 [3]. The unit cell includes 2 atoms of Tantalum (green) and 5 atoms of Oxygen (red).

First results

Firstly, the experimentally measured cell parameters are in good agreement with the theoretically calculated values with deviations less than 1 %.

In addition, our results indicate remarkable differences between the investigated phases regarding their linear optical responses. E.g. from dielectric function we observe differences between the phases regarding the positions of the main absorption edges. Therefore, it should be possible to differentiate between crystal structures of Ta_2O_5 by optical measurements, e.g. by comparing their absorption spectra.

Conclusions

As the first results are in good agreement with the experiment and in addition predict optical differences between different phases, they could be quite useful to identify crystalline structures of Ta_2O_5 by their optical properties. Additional calculations with a higher precision will be performed for a better quantitative comparison with experimental results.

References

[1] G. Kresse and J. Furthmüller, Computational Materials Science **6**, 15 (1996)
[2] G. Kresse and J. Furthmüller, Phys. Rev. B **54**, 11169 (1996)
[3] R. Nahed et al., Phys. Chem. Chem. Phys. **15**, 1352 (2013)

Photoinduced Displacement of Ferroelectric Nematic Liquid Crystal Droplets on the Surface of Lithium Niobate

Coda, Virginie[1]; Cmok, Luka[2]; Sebastián, Nerea[2]; Mertelj, Alenka[2]; Aya, Satoshi[3]; Huang, Mingjun[3]; Zgonik, Marko[2]; Montemezzani, Germano[1] and Drevenšek-Olenik, Irena[2,4]

[1]Université de Lorraine, CentraleSupélec, LMOPS, Metz, France
[2]J. Stefan Institute, Department of Complex Matter, Ljubljana, Slovenia
[3] South China University of Technology, Guangzhou, China
[4]University of Ljubljana, Faculty of Mathematics and Physics, Ljubljana, Slovenia

Introduction

The recent discovery of nematic liquid crystal molecules showing a ferroelectric order has marked a breakthrough in liquid crystal science [1,2]. In nematic liquid crystals the rodlike molecules align parallel to each other. However, the conventional nematic phase is not polar, as in average half of the molecules have their dipoles pointing in each of the two opposite directions associated to the director axis. On the contrary, ferroelectric nematic liquid crystals (FNLC) are polar fluids with alignment of their dipoles. In this work, we studied interaction of FNLCs with photovoltaic and/or pyroelectric fields generated on the surface of iron-doped lithium niobate crystals ($LiNbO_3$:Fe or LN) without requiring electrodes. When sessile droplets of a FNLC are placed onto the surface of an illuminated or heated/cooled x-cut $LiNbO_3$:Fe crystal, intriguing dynamic processes occur, such as strong flow of liquid crystalline material parallel to the direction of the photo-induced electric field.

Experimental results

An example of the observed dynamic processes, by using the DIO liquid crystal [1,3], is reported in Figure 1. In this experiment, the surface of the photorefractive LN crystal is pre-illuminated with a 532-nm laser beam focused in only one direction with a cylindrical lens to induced a space charge field perpendicular to the c-axis. Afterwards, DIO droplets are deposited on this surface. The LN crystal with DIO droplets is then placed under a polarizing optical microscope and is heated up until melting and then it is cooled down to a nematic phase. The different images of Figure 1 represent the evolution of FNLC droplets during cooling from 110°C to about 80°C with a temperature ramp of -5°C/min. The stripe-shaped region corresponding to a pseudo-permanent photo-induced refractive index change is highlighted in green. At first, the droplets change their shape from spherical (Figure 1(a)) to extended ellipsoidal (Figure 1(b)). Then, they start to rapidly move preferentially parallel to the direction of the crystal's plus and minus c-axis Figure 1(b and c). During this motion, several droplets merge into running streams extending towards the edges of the crystal. When the temperature is stabilized, the flow becomes weaker and the channels narrower (Figure 1(d)). Finally, practically all liquid-crystalline material is transferred from the top surface to the side or to the bottom surface of LN. This can be noticed in Figure 1(c) as a change of image from dark to bright.

This change in the transmitted light intensity is caused by the FNLC travelling under the crystal, which disappears out of frame of the camera in Figure 1(d). The liquid jets are mostly oriented along the crystal *c*-axis, parallel to the evanescent static electric field generated on its surface by pyroelectric and/or photovoltaic effects.

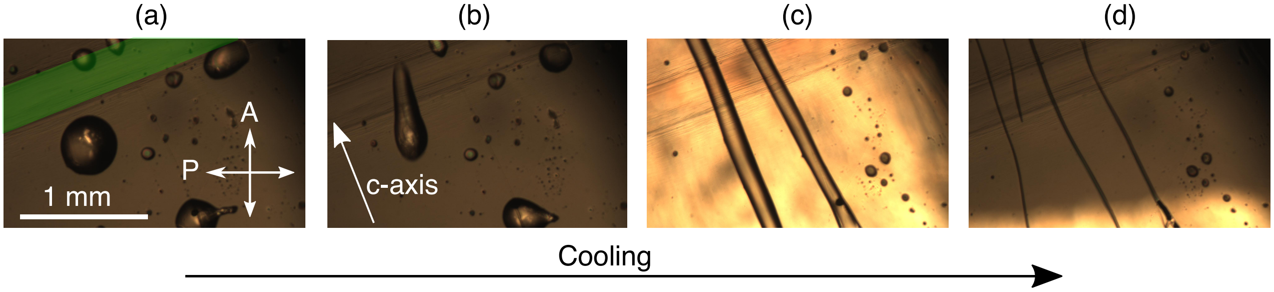

Figure 1: Example of strong displacement of DIO, a ferroelectric nematic liquid crystal, initiated by photo-induced electric field on the surface of $LiNbO_3$:Fe crystal while cooling down the crystal. Sessile droplets around 110°C (a), the droplets start to elongate (b) and abruptly transform into strong running streams (c), which become weaker when the temperature starts to stabilize around 80°C (d). The oblique region pre-illuminated by a 532-nm laser (perpendicular to the crystal's c-axis) presenting a photo-induced refractive index change is on the top left and can be seen in all images (highlighted in green in Fig.1a).

Conclusions

The observed phenomena depend on the optical field intensity, polarization, and spatial profile, and on the temperature ramp (inducing pyroelectricity). They are observed in the ferroelectric nematic phase, in the intermediate phase(s) and also in the standard nematic phase. Some dynamic processes also take place in the isotropic phase. We found that the above-described intriguing effects are reproducible also with other ferroelectric nematic liquid crystals. The strong and fast displacement of the material is initiated by the interaction of electrically charged/polarized fluid with charged surface of the photovoltaic LN crystal when electrostatic repulsion exceeds the surface tension of the fluid. Our results are in accordance with the results of very recent experiments conducted with FNLC RM257 on the LN surface initialed by pyroelectric field [4].

Acknowledgements: We acknowledge financial support of ARRS (grant P1-0192), and founding within bilateral project Bi-FR/19-20-PROTEUS-002.

References

[1] H. Nishikawa, K. Shiroshita, H. Higuchi, Y. Okumura, Y. Haseba, S. Yamamoto, K. Sago, and H. Kikuchi, Advanced Materials **29**, 1702354 (2017)
[2] N. Sebastián, L. Cmok, R. J. Mandle, M. R. de la Fuente, I. Drevenšek Olenik, M. Čopič, and A. Mertelj, Phys. Rev. Lett. **124**, 037801 (2020)
[3] H. Nishikawa and F. Araoka, Advanced Materials **33**, 2101305 (2021)
[4] R. Barboza, S. Marni, F. Ciciulla, F. A. Mir, G. Nava, F. Caimi, A. Zaltron, N. A. Clark, T. Bellini, and L. Lucchetti, to appear in PNAS (2022)

Photorefractive soliton synapsis for Surface-Plasmon-Polariton circuits

Tari Hamed,[1] Bile Alessandro,[1] Iodice Mario[2], Fazio Eugenio[1]
[1] Department of Basic and Applied Science for Engineering, Sapienza University of Rome, Italy
[2]Institute of Applied Sciences and Intelligent Systems, National Research Council, Naples, Italy

Introduction

By exploiting the typical functional geometries of the nervous system, information can be stored and processed in the same physical location, unifying memory and processor. This last aspect requires the use of modifiable plastic materials that are capable of assuming different behaviors depending on the information to be stored. Up to our knowledge, most of the platforms that have been introduced as photonic or electronic neural networks, are fixed structures that rigidly perform the calculation without the capability of changing the interconnections as requested[1]. In these structures, the configuration of the neurons and their interconnections are written and predefined. So they are only capable of doing certain limited functions, whereas the biological neurons can dynamically modify the interconnections in the process of training. They can establish new interconnections or if requires they can diminish or strengthen the weight of specific interconnections in synaptic points. This behavior is called the plasticity of the biological neurons which makes them distinguished from the most photonic and electronic neural networks that are demonstrated in the literature[2]. Also, these interconnections have a specific lifetime and their weight's strength is dependent on the extent of their exploitation. In another word, the interconnection's existence and strength is a self-driven process in which the signal itself can reconfigure its pathway by its occurrence redundancy.

Inspired by the biological neurons, we have successfully demonstrated this plasticity feature with a fully optical system[3]. However, to have a link between the electronic counterpart and also increase the number density of the neurons in the network, we have introduced a new hybrid structure that benefits the advantages of both of them simultaneously. Here the hybrid Plasmonic-Solitonic neuron takes into account both the high bandwidth and high speed of the photonic technology and also the smaller wavelength and higher interaction of electrons with the electronic platforms. However, since the Plasmonic systems have an intrinsically higher loss due to the joule effects, so their long-range propagation also is a challenging issue. Fortunately, this hybrid platform provides the long-range and low-loss propagation of the Surface Plasmon Polariton (SPP) signal via coupling it to the soliton interconnections. As a result, long-range propagation of the SPP signal is possible with negligible losses in the range of 0.04-0.07 dB/cm[4] by coupling it to the soliton.

In this study, we have demonstrated the time evolution of the soliton formation through the diffraction profile of the SPP signals via the self-focusing process in the SBN crystal. The donors (Ce^{3+}) introduced as dopants in the SBN crystal, will be transformed into the acceptors (Ce^{4+}) by absorption of the SPP diffracted light (λ=532 nm) at the end of the strip. As indicated in Fig.1A, the electrons are drifted from the beam location to the top surface of the crystal which is the ITO electrode (anode) deposited. It should be noted that the ionized donors will induce an electric field in the opposite direction of the bias applied field and as a result, the refractive index of the photorefractive material at beam location will increase with respect to the dark area through Eq.1.

$$n = n_e - \frac{1}{2} n_e^3 r_{33} \left(\overrightarrow{E_b} + \frac{\vec{D}_{sc}}{\varepsilon_{PR}}\right) \frac{1}{1+\frac{I}{I_{sat}}} \qquad \text{Eq.(1)}$$

This phenomenon gradually forms a solitonic channel and provides the long-range low loss propagation of the SPP signals which is represented through the power profile of the SPP in the frequency domain in Fig.1B. The saturation behavior of the refractive index provides the possibility to realize a sigmoid-type activation function utilizable as a decision-making element in the synaptic points. Since the formation of the solitonic channel requires successive iterations of the signal through the specific channel(represented as the inset plot in Fig.1C), hence, every signal propagation history will be memorized as a refractive index modulation in the photorefractive material and after a while, the further enhancement of the refractive index will be saturated and reaches a plateau. Considering this phenomenon, the processing in the memory will be possible with the aid of solitonic channel formation by counterbalancing effect of the diffraction and self-focusing processes.

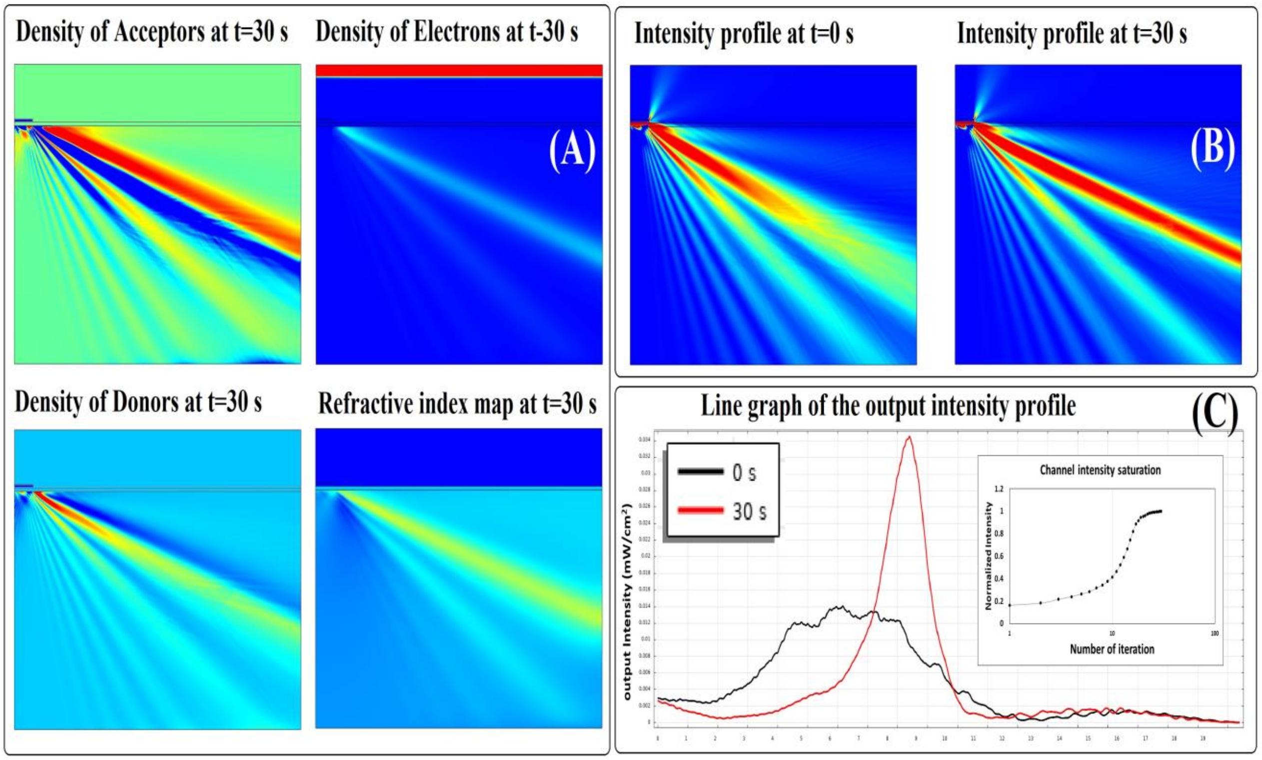

Fig.1, (A) Donors, acceptors, and electrons density at time t=30 sec along with the refractive index profile, (B) Intensity profile of the diffracted light of the SPP before and after the generation of the soliton at t=30 s, (C) Line graph of the intensity profile at the output interface of the SBN crystal at t=0 and t=30 sec after the solitonic channel formation, inset plot indicates the saturation behavior of the solitonic channel formation which follows a sigmoid shape logistic function

References

[1] Zarei, S., M.-r. Marzban, and A. Khavasi, Optics Express, 2020. **28**(24): p. 36668-36684.
[2] Song, Z.W., et al., Optics express, 2020. 28(2): p. 1561-1573.
[3] Bile, A., et al., Neural Computing and Applications, 2021: p. 1-9.
[4] Fazio, E., et al., Rom. Rep. Phys, 2013. 65(3): p. 878-901

Polar oxide nanomaterials - an emerging playground in ultrafast photophysics

Mirco Imlau[1,2]

[1]Department of Physics, Osnabrück University, Germany
[2]CellNanOs - Center for Cellular Nanoanalytics (www.cellnanos.uos.de), Osnabrück University, Germany
Barbarastraße 7, 49076 Osnabrück, DE
@ImlauLabs (Twitter, LinkedIn); https://www.mimlau.de; mimlau@uos.de

Introduction

Volume single crystals of the niobate or tantalate family are established as central workhorses in the research field of photorefraction from its very beginning. A proper control of the initial photogeneration processes yielding a directed photogalvanic current density requires homogeneous, i.e. cluster-free doping with impurity atoms (such as $\mathrm{Fe}_{\mathrm{Li}}^{2+/3+}$) within the entire volume. The dimensions of the photorefractive crystal on the mm-length scale have strong impact on key photophysical quantities, such as the efficiency, angular and/or wavelength sensitivity of recorded mixed gratings in holographic applications, but also on experimental parameters (such as the intersection angle of reference and signal beams to adjust for the grating vector of the incident light intensity pattern) or the experimental access - be it in the context of the optical detection of transmitting beams in multiwave mixing or for the electrical tapping of surface charges. Some of the early applications (e.g. holographic data storage) inevitably required large scale, homogeneous crystalline materials. Accordingly, research on single crystal growth, preparation and characterization of polar oxide crystals with high bulk homogeneity (doping, composition) and quality, commonly associated with a lack of grain boundaries, cracks, unwanted defect centers, but also a high optical quality of the surfaces ($< \lambda/20$) is closely related to the research and application field of photorefraction.

In the era of nanotechnology, the establishment of top-down material processing methods, such as micro-mechanical drilling or ion beam enhanced etching, has significantly expanded the possibilities to tailor niobate and tantalate single crystals for new type of applications, particularly in the domain of micro- and nanophotonics. Examples include whispering gallery mode resonators with sub-mm diameters enabling impressive quality factors for sensing (by the Buse group, Freiburg, Germany), free-standing ultrathin lithium niobate membranes with layer thickness down to 200 nm for integrated photonic chips (by the Tünnermann group, Jena, Germany) or niobate layer systems, e.g. lithium niobate on silicon oxide (insulator) on silicon (substrate) with lithium niobate film layers down to 300 nm for optoelectronic devices ('LNOI' by nanoLN inc., Japan). As a consequence of the reduced length scale, the requirements for single crystal homogeneities and qualities changed, and the optical properties profited from the nanostructuring rather than from doping.

These developments directed our attention to photophysical processes in nanoscaled niobates on a microsopic level. For instance, the question about the existence of the photogalvanic effect in doped niobate nanomaterials with dimensions in the sub-20-nm region is still not answered. While the persistence of the spontaneous polarization down to the sub-5 nm length scales has been validated in several representatives of the perovskite-like polar oxidic nanocrystals (such as $\mathrm{BaTiO_3}$), information about the charge transport including small polaron hopping, but also about the build-up of space-charge fields in crystals with dimensions much below the space-charge limitation length (both in the bulk and on the surface), are missing completely in literature. Besides the availability of proper nanomaterials, it is also due to missing experimental techniques for investigations.

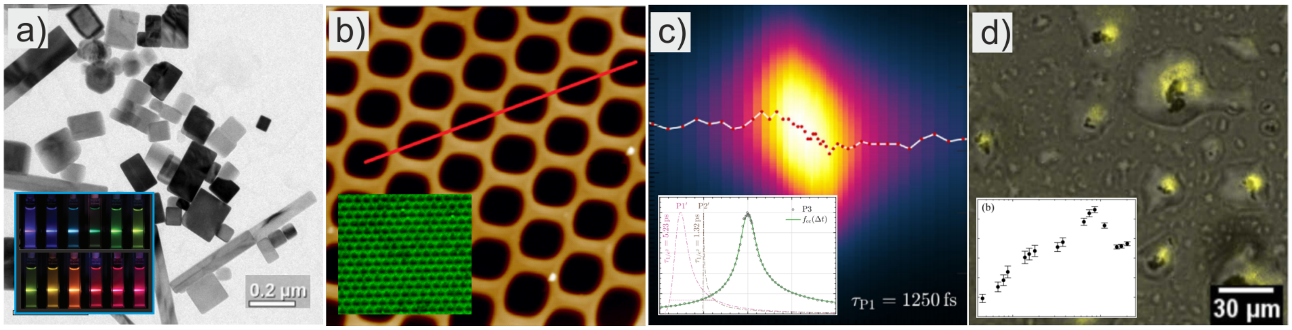

Figure 1: (a) Electron microscopy image of potassium niobate nanocrystals [1], (b) atomic force microscopic image of stamped lithium niobate metamaterials [2], (c) pulse stretching effect in nanoparticle powder pellets [3], (d) second-harmonic emission of lithium niobate nanocrystals [4]

.

This contribution gives insight to the first steps of research on nanoscale niobate crystals at Osnabrück University profiting from newly established synthesis routes for the bottom-up synthesis of nanoniobate crystals [1], stamped niobate metamaterials [2], the development of novel experimental tools based on nonlinear ultrafast spectroscopy & microscopy and reproducible preparation routes for nanoparticle powder pellets [5]. Challenges in modelling the experimental data using combined analytical and numerical tools are adressed and reveal first examples of discovered nonlinear optical phenomena directly assigned to the nanosized properties [3], but also opens the path to evaluate the impact of nanoniobates for new applications.

Acknowledgments

Contributions of all authors cited in the reference list is gratefully acknowlegded. This work was funded by the Deutsche Forschungsgemeinschaft (projects IM37/11, IM 37/12, FUGG 190/165, FUGB 190/179), by the German Federal Ministry of Education and Research (BMBF) within the funding program "Photonics Research Germany" with contract number 13N15230, the German Academic Exchange Service DAAD (projekt 57390412), the Ministry of Lower Saxonary (MWK), and the profile line 'Integrated Sciences' of Osnabrück University.

References

[1] Z. Wang, C. Kijatkin, A. Urban, M. Haase, M. Imlau and K. Kömpe, Nanoscale **10**, 10713 (2018)
[2] F. Alarslan, L. Vittadello, J. Klein, Q. Ali Khan, C. Kijatkin, M. Haase, H. Schäfer, M. Imlau and M Steinhart, Adv. Eng. Mat. (2021)
[3] C. Kijatkin, B. Bourdon, J. Klenen, L. Kocsor, Z. Szaller, M. Imlau Adv. Phot. Res. (2020)
[4] L. Vittadello, C. Kijatkin, J. Klenen, D. Dzikonski, K. Kömpe, C. Meyer, A. Paululat and M. Imlau, Opt. Mat. Exp. (2021)
[5] S. Bock, C. Kijatkin, D. Berben and M. Imlau, Appl. Sciences, **9**, 4933 (2019)

Polarization dependent second-harmonic generation in cascaded optically poled fibers

Wasyhun A. Gemechu,[1] Umberto Minoni,[1] Daniele Modotto,[1] Alessandro Tonello,[2] Vincent Couderc[2]

[1]Dipartimento di Ingegneria dell'Informazione, Università di Brescia, via Branze 38, 25123 Brescia, Italy
[2]Université de Limoges, XLIM, UMR CNRS 7252, 123 Av. A. Thomas, 87060 Limoges, France

The fortuitous discovery of effective second-harmonic generation (SHG) by Österberg and Margulis in 1986 has laid the pavement for optical poling [1]. They observed that when a Ge-doped fiber was exposed to an intense laser beam for several hours, the SH power grew exponentially before saturating after 10 hrs. This was an astounding observation, as they demonstrated an effective $\chi^{(2)} \approx 10^{-3}\,pm/V$ and a peak SHG conversion efficiency of 5%. This experimental work also paved the way for the discovery of optical poling using an external SH-seed [2] and extensive search for the physical mechanism responsible for efficient SHG in commercial optical fibers [3, 4]. Batdorf *et al.* [5] and the authors [6] demonstrated that the $\chi^{(2)}$ nonlinear grating length never exceeds 60 cm, and the onset length, where strong SH growth is observed, depends on the SH power used during seeding. Here we report, to the best of our knowledge, a novel experiment where an efficient SHG device was constructed from spliced short fiber segments poled using both linearly and circularly polarized pumps.

We conducted the SHG experiment employing a microchip Nd:YAG laser operating at 1064 nm, generating 800 ps fundamental (FF) pulses at a repetition rate of 30 kHz. A FF pump, either linearly or circularly polarized, with an average power of 36 mW, was coupled to the Corning HI980 Ge-doped fiber using an aspheric lens with 8 mm of focal length with a coupling efficiency exceeding 70%. After 15 min exposure of the fiber to both FF and type-II SH signal from a KTP crystal, the KTP was withdrawn, and the fiber continued to be poled exclusively with the FF beam. Once the SHG saturated, FF and SH powers were recorded at the exit facet of the poled fiber. We experimentally found a strong Raman spectral broadening for FF output power above 10 mW when poling a 1 m long fiber and, in order to avoid any Raman spectral broadening at the maximum pump power, we decided to pole segments as short as 20 cm. Fig.1a shows the average SH output power ($P_{SH_{avg}}$) measured as a function of the average FF output power ($P_{FF_{avg}}$); the SH power growth measured at the output of the 20 cm segment, that was poled by a linearly polarized pump (red curve), exhibits a quadratic dependence and is fitted with $P_{SH_{avg}} = 0.94 \times P_{FF_{avg}}^2$ (violet). In contrast, for segments poled by a circularly polarized pump (green), the SH power growth deviates from the theoretical parabola, and the almost linear increment is well approximated by $P_{SH_{avg}} = 0.06 \times P_{FF_{avg}}^2 + 7.09 \times 10^{-3} \times P_{FF_{avg}}$ (blue). The average SH conversion efficiency ($\eta_{avg} = P_{SH_{avg}}/P_{FF_{avg}}$) at $P_{FF_{avg}} = 11.2$ mW was about 1.2% and 0.8% for fibers poled by a linear and circular polarization, respectively.

In order to achieve a nonlinear quadratic grating longer than the onset length and to boost SH conversion efficiency, we poled several 20 cm long fibers and spliced them together. Moreover, to gain an insight into the role of polarization, we carried out the poling process utilizing either a linearly polarized (Fig.1b) or circularly polarized (Fig.1c) pump. Once the poling process was completed, before splicing, we measured the SH power at the output of each segment, verifying that all the pieces had comparable conversion efficiencies (an example is reported for two fiber segments in Fig.1b and Fig.1c: black and green graphs). Then, the segments were spliced with negligible insertion loss and the total spliced fiber length was limited to 60 cm to mitigate the detrimental effect of Raman-

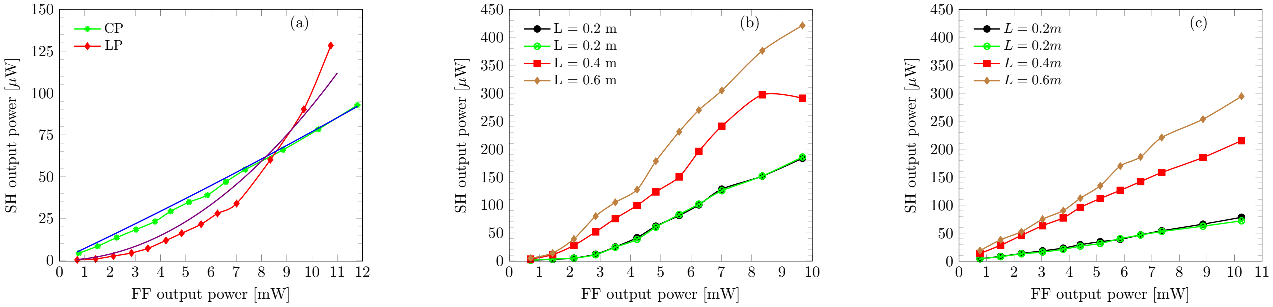

Figure 1: (a) SH output power growth as a function of the FF output power for fiber poled by a linearly (red) and circularly (green) polarized pump. Output SH (P_{SHavg}) versus FF power (P_{FFavg}) for different lengths of spliced fibers corresponding to 1,2,3 segments, each having a length of 0.2 m, poled using (b) a linearly polarized and (c) a circularly polarized pump.

induced pump depletion. We marked the fibers before removing them from the poling stage to be able to approximately preserve, during splicing, the orientation between each segment and the initial FF beam used for poling. In this regard we observed that when poling a 20 cm fiber by using a linearly polarized pump the FF output was still linearly polarized whereas the SH was elliptically polarized. Fig. 1b and Fig.1c show the SH power obtained from a single 20 cm long poled fiber and subsequently joined 2 and 3 poled segments. The conversion efficiency value obtained from 3 spliced segments (brown) poled by the linearly polarized pump is $\eta_{avg} = 4.35\%$ at $P_{FF_{avg}} = 9.67$ mW, about 2.3 times that of a single segment (green). Note that this value is less than the theoretically expected increment of 9 under ideal conditions. Similarly, for segments poled using a circularly polarized pump, the conversion efficiency is 2.87%, which is about 3.8 times that of a single 20 cm segment. We also observed that the conversion efficiency of 60 cm long poled fibers is similar to that of 20 cm poled fibers, and in some tests was even smaller. For instance, in the case of a linearly polarized pump, we measured for 60 cm long fibers $P_{SH_{avg}}$ in the range $120 - 190$ μW for $P_{FF_{avg}}$ around 10 mW, to be compared with $P_{SH_{avg}} = 190$ μW shown in Fig. 1b for $P_{FF_{avg}} = 10$ mW.

In conclusion, we have reported an efficient SHG device constructed via splicing of 20 cm segments poled using both linearly and circularly polarized pump with a corresponding average conversion efficiency of 4.35% and 2.87%, respectively. We expect further improvement with polarization control between successive segments and by utilizing polarization-maintaining fibers.

References

[1] U. Österberg and W. Margulis, Opt. Lett. **11**, 516 (1986).
[2] R. H. Stolen and H. W. K. Tom, Opt. Lett.**12**, 585 (1987). **45**, 1443 (2018)
[3] D. Z. Anderson, V. Mizrahi, and J. E. Sipe, Opt. Lett. **16**, 796 (1991).
[4] E. Dianov and D. Starodubov, Quantum Electron. **25**, 395 (1995).
[5] B. Batdorf, C. Krautschik, U. Österberg, G. Stegeman, J. Leitch, J. Rotgé, and T. Morse, Opt. Commun. **73**, 393 (1989).
[6] W. A. Gemechu, U. Minoni, D. Modotto, A. Tonello, and V. Couderc, CLEO/Europe-EQEC, (2021).

Pyroelectric field-assisted domain engineering in lithium niobate and lithium tantalate using femtosecond laser pulses

Jörg Imbrock, Dominik Szalek, Simon Laubrock, Haissam Hanafi, Cornelia Denz

Institute of Applied Physics and Center for Nonlinear Science, University of Münster,
Corrensstr. 2, 48149 Münster, Germany

Introduction

Engineered domain structures play an essential role in nonlinear optics for quasi-phase-matched parametric processes [1]. There is a great interest in domain inversion techniques based on all-optical processes which do not require external electric fields [2]. Lately, promising results have been obtained in structuring the nonlinearity in lithium niobate ($LiNbO_3$) with focused femtosecond laser pulses. These include all-optical poling [3] and $\chi^{(2)}$ depletion [4, 5]. However, these methods only allow for small feature-sized domain inversion or show increased absorption with reduced efficiency. A promising approach to overcome the aforementioned limitations is based on our recently discovered pyroelectric field-assisted domain inversion process that can be used to switch ferroelectric domains in the volume of magnesium doped $LiNbO_3$ without using an external applied electric field [6]. The process works as follows (see Fig. 1). First, focused femtosecond laser pulses induce permanent defects along the polar axis. Then, the crystal is heated up above 200 °C. During cooling, the domain inversion is driven by a space-charge field that locally exceeds the threshold field of domain nucleation. After this heating-cooling cycle, ferroelectric domains are inverted below and above the defects that act as seeds. Domain inversion occurs if a certain pulse energy and defect length are exceeded. However, there is no detailed study on the role of temperature and domain spacing in this process. The latter one is essential for the fabrication of two-dimensional nonlinear photonic structures because a certain length of a reciprocal lattice vector is required for a specific quasi-phase-matching process.

Here, we examine the pyroelectric field-assisted domain inversion in $LiNbO_3$:Mg, dependent on the temperature for 2D rectangular lattices of different periods. We measure the fraction of domains that are inverted and the domain diameters.

Pyroelectric field-assisted domain inversion

We fabricate two-dimensional lattices of ferroelectric domains by patterning magnesium-doped $LiNbO_3$ and near-stoichiometric lithium tantalate crystals with femtosecond laser pulses ($\lambda = 1030\,\mathrm{nm}$) with a pulse width of 250 fs, a repetition rate of 1 kHz and energies of up to 400 nJ. We create on different samples 2D nonlinear photonic structures with periods of (6 µm, 10 µm, 15 µm) x 6.3 µm. The crystals are then heated to various temperatures in the range of 50 °C to 400 °C and cooled down. We investigate the effect of temperature and seed spacing on the number and size of inverted domains in $LiNbO_3$:Mg. Čerenkov second-harmonic generation microscopy allows visualizing the generated ferroelectric domains and laser-induced seeds in 3D [7]. Measurements with different electrical terminations of the crystal surfaces reveal the influence of surface charges during the domain formation process.

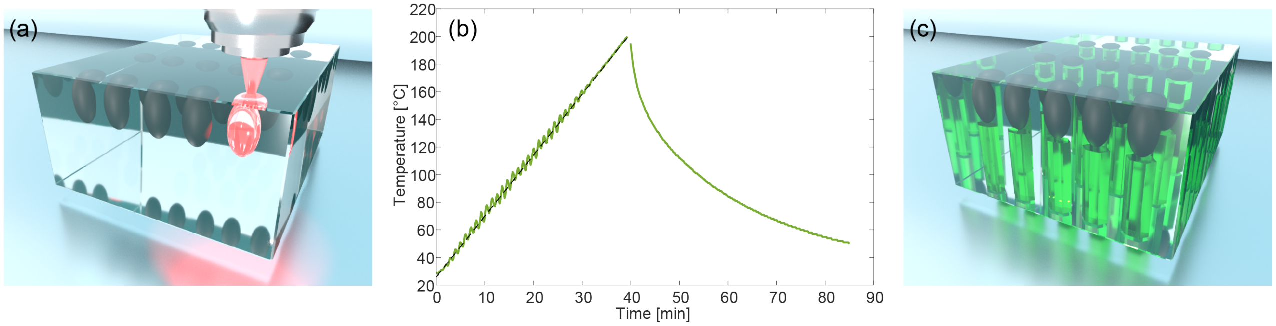

Figure 1: Scheme of the experimental procedure. (a) Permanent defects (grey) are induced with focused femtosecond laser pulses (red) along the optical axis. (b) The sample is heated to elevated temperatures and cooled down to room temperature. (c) After cooling down, ferroelectric domains (green) are inverted below and above the defects.

Conclusions

We have identified a threshold temperature and determined an optimal temperature regime between 220 °C and 300 °C in $LiNbO_3$:Mg. In this temperature range, all domains can be inverted in a 2D rectangular lattice with periods of $15\,\mu m \times 6.3\,\mu m$. Smaller lattice periods and lower temperatures result in fewer inverted domains. Above 300 °C the already inverted domains switch back in the center of the lattices. The average diameter of the central domains is approximately $2.4\,\mu m$. This size is almost independent of temperature and lattice periods. The electrical termination of the crystal surfaces has no significant influence on the domain formation process unless the crystal is completely short-circuited. In this case, no domains are inverted, indicating that surface charges are essential for the inversion process.

References

[1] A. Arie and N. Voloch, Laser Photonics Rev. **4**, 355–373 (2010).
[2] C. Ying, A. Muir, C. Valdivia, H. Steigerwald, C. Sones, R. Eason, E. Soergel, and S. Mailis, Laser Photonics Rev. **6**, 526–548 (2012).
[3] X. Chen, P. Karpinski, V. Shvedov, K. Koynov, B. Wang, J. Trull, C. Cojocaru, W. Krolikowski, and Y. Sheng, Appl. Phys. Lett. **107**, 141102 (2015).
[4] D. Wei, C. Wang, H. Wang, X. Hu, D. Wei, X. Fang, Y. Zhang, D. Wu, Y. Hu, J. Li, S. Zhu, and M. Xiao, Nat. Photonics **12**, 596–600 (2018).
[5] J. Imbrock, L. Wesemann, S. Kroesen, M. Ayoub, and C. Denz, Optica **7**, 28 (2020).
[6] J. Imbrock, H. Hanafi, M. Ayoub, and C. Denz, Appl. Phys. Lett. **113**, 252901 (2018).
[7] Y. Sheng, A. Best, H.-J. Butt, W. Krolikowski, A. Arie, and K. Koynov, Opt. Express **18**, 16539 (2010).

Quantum-analogy-based solutions for robust photonics

Germano Montemezzani[1]

[1]Université de Lorraine, CentraleSupélec, LMOPS, 57000 Metz, France

The equations describing the evolution dynamics of coupled few levels quantum systems bear direct analogy with those describing several processes in classical wave optics, including the cases of evanescently coupled waveguides, polarization transformation optics, and nonlinear optical frequency conversion. This allows to exploit the same kind of robust approaches used in the quantum field in order to reach a specific target state in a highly tolerant way. From the practical point of view the tolerance can manifest itself in a strongly extended wavelength range of operation, as well as increased immunity against temperature variations and/or design errors. This talk will summarize some of our recent works in this context. The examples will involve adiabatic approaches for light transfer, mode conversion or broadband polarization selective beam splitting in waveguide optics [1-4], a simple and robust composite optical rotator for polarization optics [5], and composite approaches for broadband nonlinear optical frequency conversion based on segmented crystals [6-8]. In the case of coupled waveguides, in some cases it is possible to test the concepts directly on light-induced waveguide structures written by means of a proper side illumination in a photorefractive material, such as $Sr_xBa_{1-x}Nb_2O_6$.

We will also discuss non-Hermitian systems, involving dissipation, that can be useful for specific purposes. An example concerns classical analogies to three-state (Λ-type) coupled quantum systems with a decaying intermediate state (see Fig. 1a). Here the input population can be represented as a superposition of so called “bright” and “dark” states, with only the dark state surviving the interaction. Such a concept can be applied to a system of three planarly arranged parallel coupled waveguides with dissipation in the intermediate one, leading to ultra-broadband wave splitting in the two external ones (Fig.1b) [9]. The same kind of approach can be linked also to cascaded frequency conversion in nonlinear optics, where a signal wave is partially converted to a target wave through an auxiliary intermediate wave at a lossy wavelength [10]. It is shown that such a system can act as a stable wave splitter between the input and target waves, the latter being nearly immune to power fluctuations of the involved pump waves. In both cases, coupled waveguides and nonlinear optics, the price to pay is a sacrifice of part of the input photons, 50% in the case where an equal splitting ratio is desired.

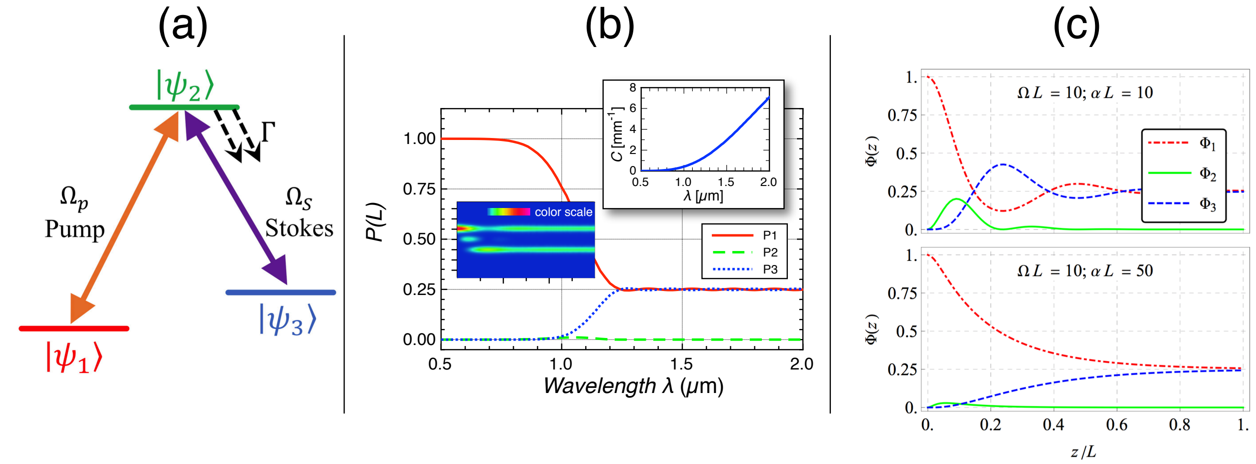

Figure 1: Non-Hermitian quantum system and two analogs in classical optics. (a) Λ-type three-state system with decaying intermediate state (decay rate Γ). Ω_p and Ω_s are the pump and Stokes coupling constants (Rabi frequencies). (b) Wavelength dependence of the output power in a system of three coupled parallel waveguides with dissipation in the central one. In the wavelength range above 1.2 µm the system acts as an ultra-broadband beam splitter with output in the first and third waveguide. The blue inset shows the spatial evolution of the wave in the waveguides (from left to right) simulated by the beam propagation method (BPM) at λ=1.5 µm. The top inset shows the wavelength dependence of the coupling constant C between neighboring waveguides. (adapted from [9]) (c) Cascaded nonlinear conversion (splitting) from an input signal wave (photon flux Φ_1) to a target wave (photon flux Φ_3) through a dissipated intermediate wave (photon flux Φ_2, amplitude absorption constant α). The graphs show the spatial evolution towards the steady-state for two values of the normalized absorption constant. The same final state with 25% of the initial photons in wave 1 and 25% in wave 3 is found in both cases. Here Ω is the effective nonlinear optical coupling coefficient assumed the same for both cascaded processes, for instance sum frequency generation (SFG) followed by difference frequency generation (DFG). Fulfillment of phase matching is assumed for both processes. (adapted from [10]).

References

[1] H. Oukraou, L. Vittadello, V. Coda, C. Ciret, M. Alonzo, A. A. Rangelov, N. V. Vitanov, and G. Montemezzani, Phys. Rev. A **95**, 023811 (2017).

[2] H. Oukraou, V. Coda, A. A. Rangelov, and G. Montemezzani, Phys. Rev. A **97**, 023811 (2018).

[3] R. Alrifai, V. Coda, A. A. Rangelov, and G. Montemezzani, Phys. Rev. A **100**, 063841 (2019).

[4] R. Alrifai, "Fonctions optiques robustes dans des structures de guides d'onde: liens avec des phénomènes quantiques", PhD Thesis, University of Lorraine, 2022.

[5] M. Al-Mahmoud, V. Coda, A. A. Rangelov, and G. Montemezzani, Phys. Rev. Applied **13**, 014048 (2020).

[6] A. A. Rangelov, N. V. Vitanov, G. Montemezzani, Opt. Lett. **39**, 2959-2962 (2014).

[7] Y. Erlich, A. A. Rangelov, G. Montemezzani and H. Suchowski, Opt. Lett. **44**, 3837-3840 (2019).

[8] M. Al-Mahmoud, V. Coda, A. A. Rangelov, and G. Montemezzani, Appl. Sci. **10**, 1220 (2020).

[9] R. Alrifai, V. Coda, J. Peltier, A. A. Rangelov, and G. Montemezzani, Phys. Rev. A **103**, 023527 (2021).

[10] M. Al-Mahmoud, V. Coda, A. A. Rangelov, and G. Montemezzani, J. Phys. B (submitted).

Real-time manipulation of microparticles in aqueous media by photovoltaic optoelectronic tweezers operating at high light intensities

Carlos Sebastián-Vicente,[1] Ángel García-Cabañes,[1,2] Mercedes Carrascosa[1,2]

[1]Departamento de Física de Materiales, Universidad Autónoma de Madrid, 28049 Madrid, Spain
[2]Instituto Nicolás Cabrera, Universidad Autónoma de Madrid, 28049 Madrid, Spain

Photovoltaic optoelectronic tweezers (PVOT) have emerged as a powerful tool for the manipulation of a wide variety of micro/nano-objects (particles, liquid droplets, bubbles or biological material) based on the electric fields induced by the bulk photovoltaic (PV) effect, often using $LiNbO_3$:Fe crystals [1, 2]. Nevertheless, the manipulation of such objects in aqueous media has remained mostly elusive so far, due to the fast screening of electrostatic fields in water. The time constant that governs the screening speed is given by $\tau_s = \varepsilon\varepsilon_0\rho$, where ε is the relative permittivity of the medium, ρ its resitivity and ε_0 the vacuum permittivity. Even in the case of ultrapure Milli-Q water, with a resistivity of 18.2 MΩ · cm at room temperature, the PV electric fields are screened in around ~100 μs, thus hindering the proper functioning of PVOT. To the best of our knowledge, only two experiments have revealed some effects in water [3, 4]. However, water is ubiquitous in biological environments, where it plays a vital role. Therefore, the successful operation of PVOT in water is of remarkable interest for potential applications in biotechnology or biomedicine, among others. An interesting approach to circumvent this constraint consists of manipulating aqueous droplets in a nonpolar medium [5-9], which may serve as carriers of particles or biological material [7]. This scheme is currently a very active field of research.

In this work, we show experimentally that it is feasible to employ PVOT in deionized Milli-Q water by using simultaneous light excitation with high intensities. A few years ago, M. Esseling developed a simple theoretical model to describe the time evolution of the PV electric field when the crystal is surrounded by a leaky medium with a non-negligible electrical conductivity [10]. In that model, the buildup of the PV electric field is given by:

$$E_{PV}(t) = \frac{E_{sat}\tau_s}{\tau_{PV}+\tau_s}\left(1 - e^{-t/\tau_0}\right) \quad (1)$$

where τ_s the screening time of the surrounding medium, τ_{PV} the PV response time (inversely proportional to the light intensity), $\tau_0 = \tau_s\tau_{PV}/(\tau_s + \tau_{PV})$ is the effective time constant and E_{sat} is the saturation PV field when the surrounding medium is not leaky (i.e. $\tau_s \rightarrow \infty$). Thus, both the saturation PV field and the effective time constant τ_0 depend on the light intensity. Namely, the higher the intensity, the higher the saturation PV field and the faster the time evolution.

Herein, we show the successful operation of PVOT using high intensities of around ~1 kW/cm^2. At such intensities, the screening time of water is not negligible compared with the PV buildup time, allowing for the generation of an evanescent electric field (which persists as long as light excitation is maintained). A representative result on a *z*-cut substrate, using micro-clusters of silver nanoparticles with diameters of ~100 nm, is shown in Figure 1 for two light intensities. For the lower intensity a disk-like trapping pattern can be observed at the center of the light spot, whereas a ring-like shape occurs for the higher intensity. These results could be explained by recently reported numerical simulations of the dielectrophoretic forces exerted by PVOT when operating with *z*-cut substrates [11]. Nevertheless, the additional interplay of optical or thermal effects cannot be disregarded at such high intensities, and further investigation is required.

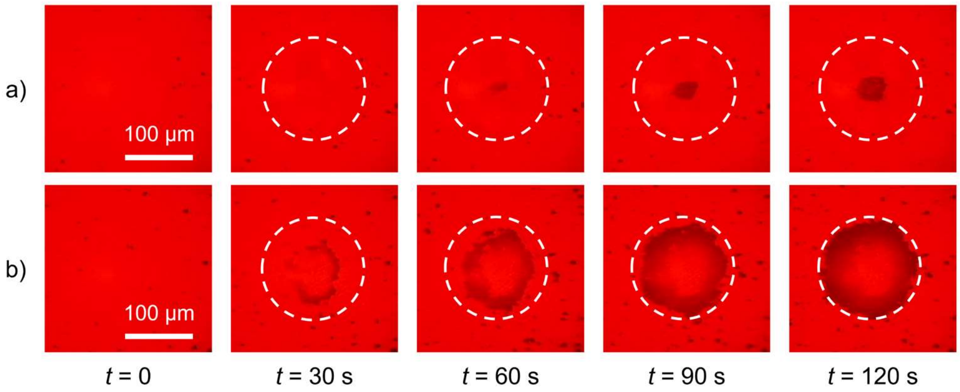

Figure 1: Time sequence of silver particle trapping suspended in Milli-Q water on a *z*-cut $LiNbO_3$:Fe substrate. At $t = 0$ the substrate is illuminated with a Gaussian light beam ($\lambda = 532$ nm, $1/e^2$ diameter of 150 µm indicated by a white dashed circle), with an intensity of a) 0.97 kW/cm^2, and b) 2.0 kW/cm^2.

Furthermore, when light is switched off, the evanescent field rapidly fades away, allowing us to carry out dynamic real-time manipulation, very constrained in nonpolar liquids due to the long lifetime of the electric fields in the dark. Fruitful results with both *z*-cut and *x*-cut $LiNbO_3$:Fe crystals have been accomplished, achieving a long-sought milestone for PVOT.

Funding from the Ministerio de Economía, Industria y Competitividad (MAT2017-83951-R) and the Ministerio de Ciencia e Innovación of Spain (PID2020-116192RB-I00) is gratefully acknowledged.

References

[1] M. Carrascosa et al., Appl. Phys. Rev. **2**, 040605 (2015)
[2] A. García-Cabañes et al., Crystals **8**, 65 (2018)
[3] S. S. Sarkisov et al., Appl. Phys. Lett. **79**, 901 (2001)
[4] L. Miccio et al., Opt. Lasers Eng. **76**, 34 (2016)
[5] M. Esseling et al., Laser Photonics Rev. **9**, 98 (2015)
[6] B. Fan et al., Phys. Rev. Appl. **7**, 064010 (2017)
[7] A. Puerto et al., Phys. Rev. Appl. **14**, 024046 (2020); and Biomed. Opt. Express **12**, 6601 (2021)
[8] Y. Mi et al., ACS Appl. Mater. Interfaces **13**, 45018 (2021)
[9] A. Zaltron et al., Adv. Mater. Interfaces, 2200345 (2022)
[10] M. Esseling, Photorefractive Optoelectronic Tweezers and Their Applications, PhD thesis, University of Münster, 2015 (Chapter 5)
[11] J. F. Muñoz-Martínez et al., Opt. Express **28**, 18085 (2020)

Slowdown of nanosecond light pulses without distortion

Nacera Bouldja,[1,2] Alexander Grabar,[3] Marc Sciamanna,[1,2] Delphine Wolfersberger,[1,2]

[1]1Chair in Photonics, CentraleSupélec, LMOPS, F-57070 Metz, France
[2]Université Lorraine, CentraleSupélec, LMOPS, F-57070 Metz, France
[3]Institute of Solid-State Physics and Chemistry, Uzhhorod National University,
Pidhirna 46,88000 Uzhhorod, Ukraine

The slowdown of the light is focused on the study of the physical processes that can reduce the group velocity of a light pulse as it propagates in non-linear media. This phenomenon has been observed in several physical systems, including optical fibers[1] and photorefractive (PR) media[2]. The ability to slowdown light pulses is a fascinating phenomenon with important applications, such as optical information processing and optimization of telecommunications infrastructures. For that, the slow light phenomenon must have a large bandwidth to respond quickly to the short light pulses that will carry the data. However, in the PR crystal, only light pulses of the order of milliseconds or seconds have been slowed down, and because of the high dispersion, they are broadened at the output of the PR crystals[2, 3], leading to loss of the information.

Recently, we have demonstrated that the two-wave mixing (TWM) effect in the pulsed regime can slowdown nanosecond light pulses in a PR SPS crystal[4]. This is possible only if the laser intensity is high enough to reduce the crystal response time to the value of the input pulse duration. The experimental setup of TWM is performed with a Sb-doped SPS crystal whose dimensions are 8.x8x8.1 mm^3 along the x, y, and $z-$axis. The beam laser is split into two arms corresponding to the pump and signal pulses with the same duration ($t_0 = t_p$). The two light pulses interfere in the PR sample and create a refractive index grating as it is shown in Fig. 1(a).

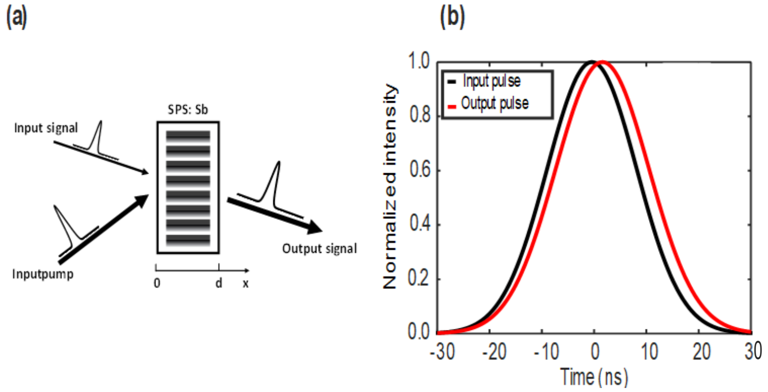

Figure 1: a) Geometric scheme of the two-wave mixing in the pulsed regime in a PR SPS: Sb crystal with thickness $d = 0.8$ cm and response time of $\tau = 32$. b): Experimental result of the temporal envelopes of the normalized input (black line) and output (red line) pulses as a function of the time, time delay $\Delta\tau = 2$ ns for a light pulse with a width $t_0 = 20$ ns and a coupling strength $\Gamma d = 5$.

By analyzing the intensity profiles of the signal pulse at the input and the output of the PR crystal, we note that the output pulse is amplified and its maximum is shifted in time compared to the input one. As we reported in[4], this configuration can achieve a maximum PR gain of the order $\Gamma = 7$

cm^{-1} and decrease the response time of the PR crystal to a value of $\tau = 32$ ns. In this case, we have successfully slowed down pulses with durations t_0 which vary between 10 to 100 ns with time delays of 1 to 25 ns. On the other hand, we note that TWM with a pulsed laser allows decelerating nanosecond light pulses and limits their distortion at the output of the crystal. As is shown in Fig. 1(b), for a coupling strength of $\Gamma d = 5$ and a response time of $\tau = 32$, a pulse of 20 ns can be delayed by 2 ns without distortion[4].

To understand why the pulse propagates in the crystal without broadening in the case of the TWM in the pulsed regime, a theoretical study has been performed. This consists in the analysis of the influence of the pump pulse duration on the slow light performances using the Eq. (14) of [5]. Fig. 2 shows the temporal envelopes of the normalized output pulses as a function of the normalized time (t/τ). The result is plotted for $\Gamma d = 5$, $t_0/\tau = 0.6$ ($t_0 = 20$ ns and $\tau = 32$ ns) and three values of the pump width (($t_p/\tau = 0.4$, 0.6, 2). As is shown in Fig. 2, we note that the normalized time delay $\Delta\tau/\tau$ and the output pulse duration t_1/τ depend on the value of t_p/τ. Indeed for large values of the pump duration ($t_p/\tau \leq t_0/\tau$), no widening is calculated but the delay is smaller. However, if we increase the pump width, both the time delay and the widening become important.

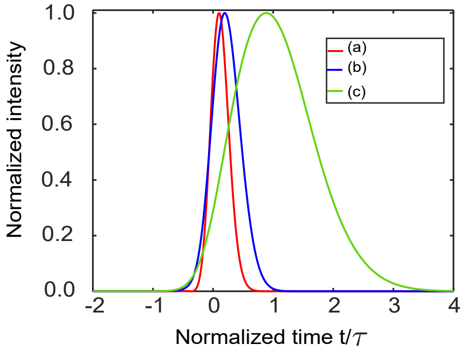

Figure 2: Temporal envelopes of the normalized output pulses as a function of the normalized time, with $\Gamma d = 5$, $t_0/\tau = 0.6$. a): $t_p/\tau = 0.4$, $\Delta\tau/\tau = 0.1$ ns and normalized output pulse duration $t_1/\tau = 0.3$. b) $t_p/\tau = 0.6$, $\Delta\tau/\tau = 0.2$ ns and normalized output pulse duration $t_1/\tau = 0.5$. c) $t_p/\tau = 2$, $\Delta\tau/\tau = 0.9$ ns and normalized output pulse duration $t_1/\tau = 1.7$, the result is obtained using the Eq. (14) of [5].

In conclusion, we have demonstrated that the SPS crystal can slow down nanosecond light pulses using a TWM method in the pulsed regime. Also, the theoretical studies show that the signal pulse can propagate in the PR crystal without distortion if its width is equal to or larger than the pump pulse duration. Finlay, our results show that, besides the PR gain, the pump pulse duration is another key parameter that can control the slow light performances.

References

[1] Baba, T. Slow light in photonic crystals. Nature photonics 2, 465 (2008).
[2] N.Bouldja, A.Grabar, M.Sciamanna, D. Wolfersberger,Phys. Rev. Research 2, 032022. (2020).
[3] N. Bouldja, M. Sciamanna, and D. Wolfersberger, Opt. Lett. 44, 1496-1499 (2019)
[4] N. Bouldja, M. Tsyhyka, A. Grabar, M. Sciamanna, and D. Wolfersberger, Phys. Rev. A 105, L021501 (2022).
[5] Sturman, et al. J. Exp. Theor. Phys. 106, 668 (2008).

Small polaron hopping in $\mathrm{Fe:LiNbO_3}$ from microscopic modelling to macroscopic observables

Laura Vittadello,[1,2] Mirco Imlau,[1,2] Marco Bazzan[3]
[1]Department of Physics, Osnabrück University, Barbarastraße 7, Osnabrück, Germany
[2]Research Center for Cellular Nanoanalytics Osnabrück (CellNanOs), Osnabrück University (Germany)
[3]Physics and Astronomy Department, University of Padova and INFN, Padova (Italy)

Iron doped lithium niobate is one of the most used ferroelectric oxides for photorefractive applications, such as the realization of high quality volume gratings, optical memories, holography and integrated circuits with all-optical capabilities [1]. Nowadays, for the same motivation, it starts to gain attention as ferroelectric photovoltaic material [3].

It is already accepted that the light-induced charge transport properties in this system can be understood to a large extend in terms of small polaron hopping.

In $\mathrm{Fe:LiNbO_3}$ three different small electron polaron types are generally considered [2]: polarons localized on regular Nb sites, or free polarons (F); polarons localized on $\mathrm{Nb_{Li}}$ antisite defects (P); polarons localized on $\mathrm{Fe_{Li}}$ substitutional defects (Fe). Each of the former two can move by thermal assisted hopping among different sites, until a deep Fe trap is encountered.

Despite this advanced level of microscopic understanding, there is still a lack of knowledge on the relation between the macroscopic observable such as polaron mobility and lifetime with the basic polaron hopping processes. This missing knowledge is one of the main motivation preventing further tailoring of the mentioned applications. Here a first step in this reconciliation is proposed.

The Marcus- Holstein hopping model provides an explicit formula to compute the average hopping frequency $\omega_{i,j}$ between two different polaronic sites i and j at a given distance and for a given temperature. This formula lends itself to a numerical procedure based on a Monte Carlo approach to simulate macroscopic quantities as a result of the random motion of a statistically significant number of polaron hoppers [4]. It is possible to follow every polaron jump and keep track of its position, the time between the jumps and the different types of visited sites. These three basic information permit to reconstruct macroscopic quantities such as the polaron lifetime or the mobility, bridging the gap between the micro and the macro description.

In Fig. 1 a) a typical output is shown. In the upper part the green curve represents the survival probability of an antisite polaron created by photo-excitation. In the bottom of the figure the number of hops performed as P and F polaron are shown. The particular shape of the polaron decay is determined by the dominant polaron jumping mechanism at the different time scales [6]. At short times, it can be seen that the dominating polaron trapping mechanism (assumed to start initially on an antisite defect) involves fast direct hopping towards iron traps in one single jump, without percolation on other mobile sites. This first regime is named as *direct trapping regime.* In the long time scale, we encounter decay processes corresponding to polarons performing a certain number of hops before encountering a deep iron trap and end their life. The crossing point between the two regimes occurs at a time τ_0 corresponding to the typical time for the polaron to hop on a nearby transport site.

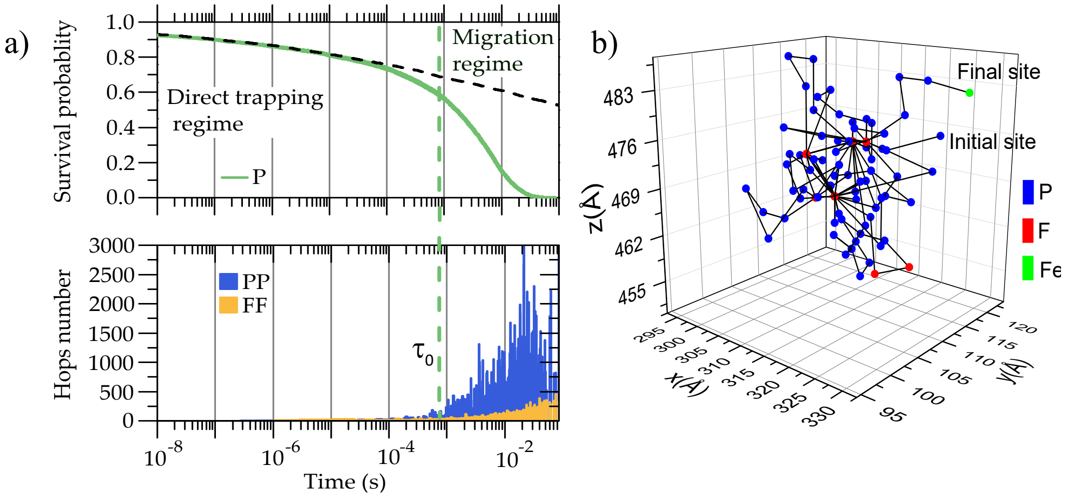

Figure 1: a) (Top) Survival probability of P polarons as measured by a typical LIA experiment. The black dashed line shows the decay shape when polaron migration is prohibited. (Bottom) Number of PP and FF hopping processes performed by each polaron during its walk.. b) Exemplary result of a polaron trajectory just after $t = \tau_0$.

After all the "quick" direct trapping processes have occurred, it becomes more probable that the polaron hops on a transport site rather than stay on its original site until a direct hop on a Fe trap takes place. An exemplary result of a polaron trajectory just after $t = \tau_0$ is shown in Fig. 1 b). This regime is indicated as *migration-accelerated regime*.

The second important macroscopic quantity that can be modelled in term of polaron hopping diffusion is the polaron mobility μ. Generally it is assumed that charge carriers are normally diffusing particles with a time independent mobility. This assumption is justified in the case of free polarons, since the distribution of the hopping times satisfies the hypothesis of the central limit theorem. However bound polarons are characterized by an heavy-tailed distribution of hopping times which lead to the so-called anomalous diffusion behaviour. In this context, mobility is a time-dependent quantity leading to unusual phenomenology for the macroscopic charge transport processes when the latter are dominated by bound polarons. Monte Carlo simulations are helpful also to investigate these regimes.

References

[1] P. Günter, J.P. Huignard. Springer, New Yorl, USA. Volume 113 (2006)
[2] O. F. Schirmer, J. Phys.: Condens. Matter **21** (2009) 123201 (29pp)
[3] H. Jiangang, F. Cesare, M. R. James, Chemistry of Materials **28**, 1 (2015)
[4] L. Guilbert, et al., J. Phys.: Condens. Matter **30**, 125701 (2018)
[5] S. Messerschmidt, et al., Optical Material Express **9**, 2748 (2019)
[6] L. Vittadello et al., Crystals 2021, **11**, 302.

Solution-deposited $BiFeO_3$ films: Photovoltaic effect & electro-optic response in dependence of doping & substrate stress

A. Blázquez Martínez,[1,2,3] N. Aruchamy,[1,2,3] S. Glinsek,[1,3] T. Granzow,[1,3]

[1]Materials Research and Technology Department, Luxembourg Institute of Science and Technology,
41 rue du Brill, 4422 Belvaux, Luxembourg
[2]University of Luxembourg, 41 rue du Brill, 4422 Belvaux, Luxembourg

Introduction

Bismuth ferrite ($BiFeO_3$, BFO) is special among perovskite-structured ferroelectrics, as it displays both ferroelectric and antiferromagnetic order. Both the high Curie temperature of more than 1000 K and the large spontaneous polarization in the order of $1\,C/m^2$ in BFO single crystals also make it attractive for basic scientific study and potential applications. Last, but not least, BFO displays fascinating photo-ferroelectric and optical properties such as a high birefringence and a pronounced anomalous photovoltaic effect. Photovoltaic conversion efficiencies several orders of magnitude higher than that for the bulk photovoltaic effect in other ferroelectrics were reported for epitaxial BFO films, spurring intensive research of BFO for photovoltaic applications [1]. For these investigations, BFO is usually in the form of epitaxial films created using vacuum deposition technologies such as pulsed laser deposition (PLD) or sputtering. A more cost-effective method to fabricate thicker BFO films is chemical solution deposition (CSD), e.g. by spin coating, typically resulting in polycrystalline films. One major drawback of these films is their comparably high conductivity, causing high leakage currents and making it difficult to achieve fully polarized samples.

Results

In this presentation, we will show how high-quality highly out-of-plane $(001)_{\mathrm{pc}}$-textured polycrystalline BFO films can be prepared by spin-coating [2]. Leakage is drastically reduced by doping with Mn and Ti, resulting in films with properties that rival those of epitaxial films. The polarization hysteresis P(E) can be measured with frequencies down to kHz and below, and leakage-corrected remanent polarization is around $0.5\,C/m^2$, about 70 % of the maximum value possible for this orientation, based on single-crystal data. A variation of the substrate material allows to modify the mechanical stress in the film, ranging from 0.54 GPa tensile to 0.93 GPa compressive stress; the variation of the ferroelectric hysteresis at different stress states is minor.

Coplanar interdigitated electrodes (IDEs) are used to achieve electrical in-plane poling. Illumination with a wavelength of 455 nm generates a short-circuit photocurrent with a current density J_{sc}. Mn-doping causes an increase of the current density to the order of several tens of $\mu A/cm^2$; the sign of J_{sc} depends on the ferroelectric polarization direction. As can be seen in Fig. 1, the films display all characteristics of a bulk photovoltaic effect: J_{sc} and photoconductivity σ_{Ph} are linear with light intensity, but the open-circuit voltage V_{OC} is independent of intensity (Fig. 1(a) & (b)), V_{OC} scales with electrode distance (Fig. 1(c)), and most importantly, J_{sc} shows a sinusoidal dependence on light polarization angle, in agreement with the tensorial nature of the bulk photovoltaic effect. There is a strong dependence of the photovoltaic effect on in-plane mechanical stress, a phenomenon that is attributed to a piezo-photovoltaic effect [4].

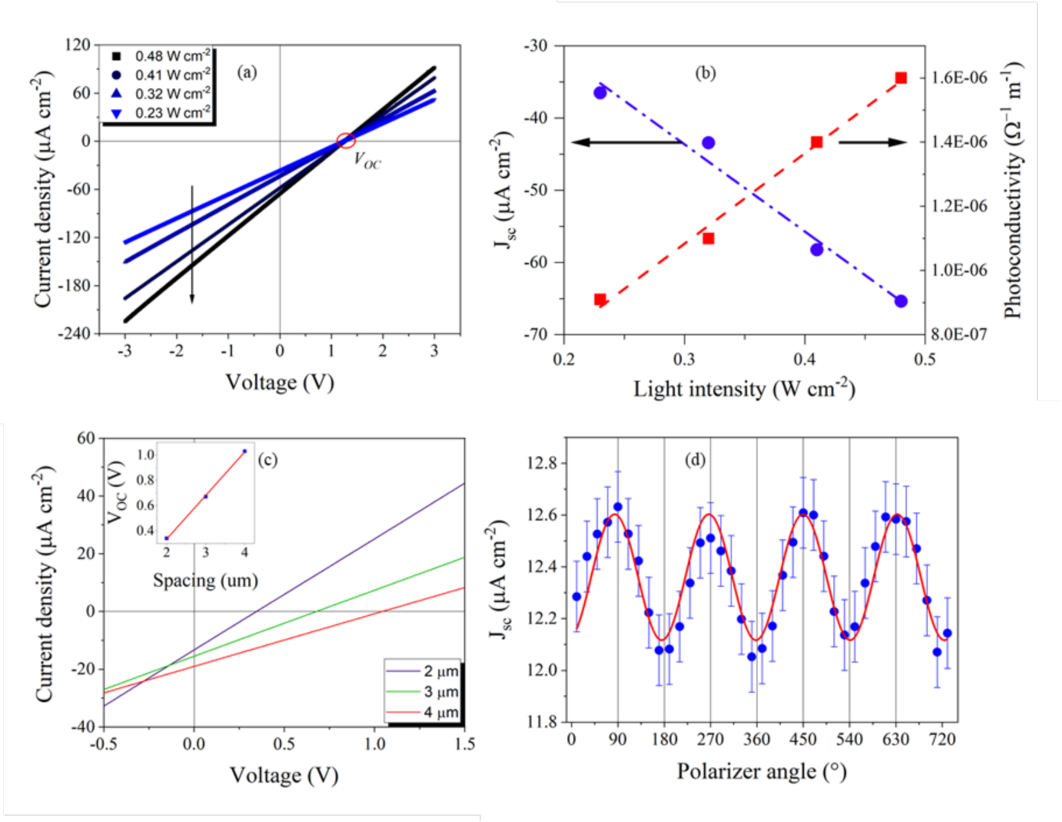

Figure 1: (a) Current-voltage curves of BFO at different light intensities. (b) Variation of J_{sc} and σ_{Ph} with light intensity (c) J-V curves of BFO with different electrode spacing (d) Variation of J_{sc} with light polarization direction at an intensity of $0.10\,\mathrm{W/cm^{-}2}$. 0° denotes the light polarization parallel to the poling direction. Reproduced from [3].

The Pockels effect of the films is quantified using a modified Teng-Man setup in transmission geometry. The values of the electrooptic tensor are notably lower than those of BFO single crystals and show little dependence on substrate stress or doping. Combined with the high photovoltaic effect and reasonable dark conductivity of the films, BFO seems a good candidate for transient photorefractive applications such as reconfigurable waveguides.

References

[1] G. Chen et al., Mater. Res. Bull. **110**, 39 (2019).
[2] Alfredo Blazquez Martínez et al., J. Eur. Ceram Soc. **41**, 6449 (2021).
[3] Alfredo Blazquez Martínez et al., Scripta Mater. **211**, 114498 (2022).
[4] S. Nadupalli et al., Sci. Adv. **5**, eaau9199 (2019).

Synthetic Magnetism in Nonlinear Photonic Crystals

Ady Arie[1]

[1]School of Electrical Engineering and the Center for Light-Matter Interaction,
Tel Aviv University, Israel

The dynamics of nonlinear sum frequency generation is analogous to spin current dynamics in magnetic fields [1]: the signal and idler complex amplitudes represent the two-dimensional spinor; the nonlinear coupling (governed by the undepleted pump and nonlinear modulation) represents the strength and direction of the magnetization; and the transverse Laplacian of the beams represent the kinetic energy. This analogy can be useful for broadband frequency conversion [2], for accumulation of geometric phase [3, 4] and its application for non-reciprocal and asymmetric beam focusing [5] and for spin-dependent deflection, representing the nonlinear-optics analogue of the Stern-Gerlach effect [6].

To realize these concepts, the second order nonlinear coefficient of the crystal should be spatially modulated. In ferroelectric crystals, this can be done by electric field poling, which enables to modulate the nonlinearity along two, out of the three axes of the crystal. A recent breakthrough enables now to modulate the nonlinear coefficient in all the three dimensions of the nonlinear crystal [7] by focusing a strong femtosecond laser to selected points in the crystal. This new method opens the door for the design and formation of skyrmionic nonlinear photonics crystals [8]. These structures would give rise to an all-optical topological Hall effect, in which the deflection of light beams depends on the spectrum and propagation direction of the input light. Furthermore, this deflection can be optically controlled by the topological charge of the pump beam.

Whereas the effects described above are observed with classical light beams, when a signal-idler frequency-superposition qubit is injected, new effects such as bunching of the two-photon state are revealed. This bunching is the frequency-domain analogue of the Hong-Ou-Mandel effect, and it opens new possibilities to control the spectral and spatial degrees of freedom of quantum light.

References

[1] A. Karnieli and A. Arie, Phys. Rev. Lett. **120**, 053901 (2018)
[2] H. Suchowski, G. Porat and A. Arie, Lasers and Photon. Rev. **8**, 333 (2014)
[3] A. Karnieli and A. Arie, Opt. Express **26**, 4920 (2018)
[4] A. Karnieli, Y. Li and A. Arie, Front. Phys. **17**, 12301 (2022)
[5] A. Karnieli, S. Trajtenberg-Mills, G. Di Domenico and A. Arie, Optica **6**, 1401 (2019)
[6] Y. Zhang, Y. Sheng, S. Zhu, M. Xiao, and W. Krolikowski, Optica **8**, 372 (2021)
[8] A. Karnieli, S. Tsesses, G. Bartal and A. Arie, Nat. Commun. **12**, 1092 (2021)

Time resolved sum-frequency generation in lithium niobate tantalate nanoparticles

Jan Klenen,[1,2] Laura Vittadello,[1,2] Bjoern Bourdon[1,2],[2] Mirco Imlau[1,2]

[1]Department of Physics, Osnabrück University, Barbarastraße 7, Osnabrück, Germany
[2]Research Center for Cellular Nanoanalytics Osnabrück (CellNanOs), Osnabrück University, Barbarastraße 11, Osnabrück, Germany

Introduction

Polar oxide, nonlinear optical (NLO) nanoparticles are essential for the further understanding of light-matter interaction and light-induced charge transport phenomena in fundamental physics on the atomic scale, but also are promising for the development of novel NLO applications in the field of nanophotonics, such as nonlinear optogenetics in life sciences [1]. Apart from their pronounced NLO coefficients, polar oxide nanoparticles with diameters much below 100 nm enable spectral tuning by means of frequency conversion without the need for phase-matching. A much reported drawback, however, is their weak conversion efficiency, connected with low signal emission, that requires sophisticated detection technologies in spectroscopy and imaging applications. For this reason, ensemble measurements are attractive, i.e., the gathering of signals from a large number of particles. An important prerequisite is the reproducible preparation of pressed nanoparticle powder pellets [2, 3]. Furthermore, developing a thorough, experimentally validated understanding of the respective fundamental processes inside the pellet, such as the question about the complex optical paths taken in disordered media, represents a challenging task that has not been adequately addressed so far.

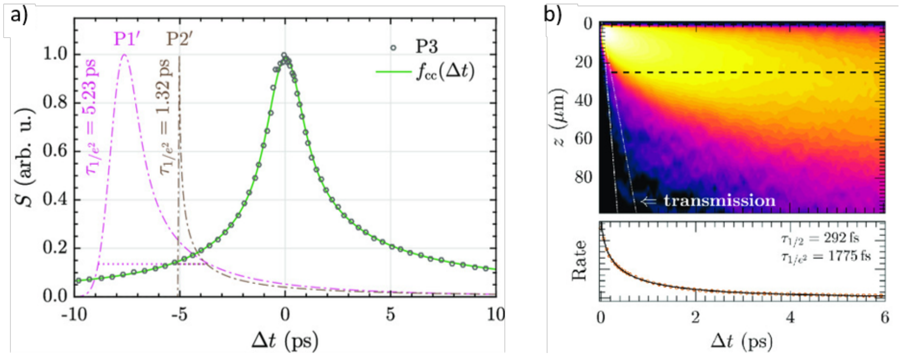

Figure 1: a) Measured SFG signal of two laser pulses ($P1$ and $P2$) in a HNP powder pellet as a function of temporal delay Δt between the two (circles) for pulse durations $\tau_{P1} = 1250$ fs and $\tau_{P2} = 44$ fs. b) Simulation of the scattering events per 60 fs time intervals at different depths inside the medium and the retrieved temporal pulse profile at a corresponding depth of 25 μm.

In this contribution, we focus on the particular case of ultrashort laser pulse propagation inside powder pellets of polar oxide, NLO nanoparticles and study the impact of composition in the solid solution $\mathrm{LiNb_{1-x}Ta_xO_3}$ (LNT) with $0 < x < 1$) including the prominent edge compostions $\mathrm{LiNbO_3}$ ($x = 0$) and $\mathrm{LiTaO_3}$ ($x = 1$) [4, 5]. By recording the time-resolved sum-frequency generation (SFG) signal and by performing numerical studies incorporating multiple scattering and superdiffusive light propagation, we are able to retrieve temporal profiles of incident laser pulses on a sub-picosecond timescale (see Fig. 1).

This way, we are also able to predict the influence of pellets with differently sized particle distributions. Experimental validation is carried out within the framework of a series of measurements with particle sizes ranging from 50 to 400 nm. Moreover the influence of NLO properties on the pulse propagation is investigated. For instance, the pulses temporal evolution in pellets composed of LNT particles with different compositions x is monitored. We explore the possibility to apply our findings for short-pulse characterization, e.g., the determination of the chirp parameters usually determined from sophisticated femtosecond wave-mixing methods (see Fig. 2).

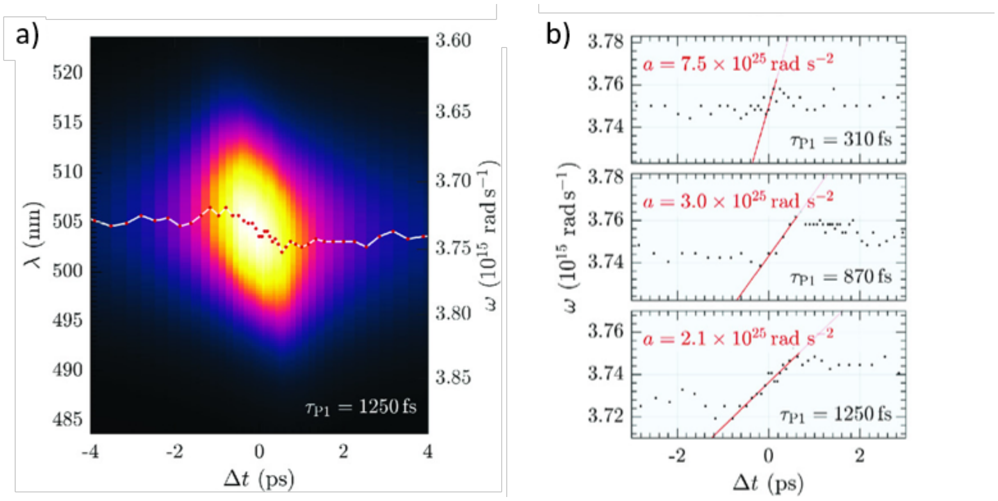

Figure 2: a) Instantaneous spectra of the SFG as a function of the temporal delay Δt between two differently colored pulses; respective maximums are highlighted by a dash-dotted line. b) Linear chirp parameter of the SFG with one initial pulse $P1$ being stretched to 310, 870, and 1250 fs.

Acknowledgments

Contributions of all authors cited in the reference list is gratefully acknowlegded. This work was funded by the Deutsche Forschungsgemeinschaft (DFG FOR5044 IM7/12, DFG INST FUGG 190/165-1).

References

[1] L. Vittadello, C. Kijatkin, J. Klenen, D. Dzikonski, K. Kömpe, C. Meyer, A. Paululat, and M. Imlau, Opt. Mater. Express, **11**, 1953-1969 (2021)

[2] C. Kijatkin, J. Eggert, S. Bock, D. Berben, L. Oláh, Z. Szaller, Z. Kis, M. Imlau, Photonics, **4**, 11 (2017)

[3] S. Bock, C. Kijatkin, D. Berben and M. Imlau, Appl. Sciences, **9**, 4933 (2019)

[4] C. Kijatkin, B. Bourdon, J. Klenen, L. Kocsor, Z. Szaller, M. Imlau, Adv. Phot. Res. (2020)

[5] L. Vasylechko, V. Sydorchuk, A. Lakhnik, Y. Suhak, D. Wlodarczyk, S. Hurskyy, U. Yakhnevych, Y. Zhydachevskyy, D. Sugak, I.I. Syvorotka, I. Solskii, O. Buryy, A. Suchocki, H. Fritze, Crystals, **11**, 755 (2021)